© 2022. Published by The Company of Biologists Ltd | Development (2022) 149, dev200082. doi:10.1242/dev.200082

RESEARCH ARTICLE

PRDM paralogs antagonistically balance Wnt/β-catenin activity during craniofacial chondrocyte differentiation

Lomeli C. Shull[1], Ezra S. Lencer[1], Hyun Min Kim[2,‡], Susumu Goyama[3], Mineo Kurokawa[4], James C. Costello[2], Kenneth Jones[5,*] and Kristin B. Artinger[1,‡,§]

ABSTRACT

Cranial neural crest cell (NCC)-derived chondrocyte precursors undergo a dynamic differentiation and maturation process to establish a scaffold for subsequent bone formation, alterations in which contribute to congenital birth defects. Here, we demonstrate that transcription factor and histone methyltransferase proteins Prdm3 and Prdm16 control the differentiation switch of cranial NCCs to craniofacial cartilage. Loss of either paralog results in hypoplastic and disorganized chondrocytes due to impaired cellular orientation and polarity. We show that these proteins regulate cartilage differentiation by controlling the timing of Wnt/β-catenin activity in strikingly different ways: Prdm3 represses whereas Prdm16 activates global gene expression, although both act by regulating Wnt enhanceosome activity and chromatin accessibility. Finally, we show that manipulating Wnt/β-catenin signaling pharmacologically or generating *prdm3*$^{-/-}$;*prdm16*$^{-/-}$ double mutants rescues craniofacial cartilage defects. Our findings reveal upstream regulatory roles for Prdm3 and Prdm16 in cranial NCCs to control Wnt/β-catenin transcriptional activity during chondrocyte differentiation to ensure proper development of the craniofacial skeleton.

KEY WORDS: Prdm3, Mecom/Evi1, Prdm16, Neural crest, Craniofacial, Wnt/β-catenin, Zebrafish, Mouse

INTRODUCTION

Cranial neural crest cells (NCCs) give rise to chondrocytes that will form cartilaginous structures to provide the foundation for the craniofacial skeleton. The growth of these cartilage scaffolds depends on chondrocyte organization and positional orientation, which facilitates proper transitions from proliferative states towards hypertrophy and the eventual recruitment of osteoblasts to deposit bony matrices (Kimmel et al., 1998, 2010; Keller et al., 2000; Hall, 1978a; Le Pabic et al., 2014). These processes require extensive temporal and spatial regulation as alterations to the gene regulatory networks (GRNs) and signaling modules that control craniofacial chondrocyte maturation can impact the development of these structures and contribute to craniofacial defects (Biosse Duplan et al., 2016; Chai et al., 2000; Keith, 1910; Lei et al., 2016; Manocha et al., 2019; Ramaesh and Bard, 2003; Ricks et al., 2002; Svandova et al., 2020; Wilson and Tucker, 2004; Hall, 1978b).

Canonical Wnt/β-catenin signaling plays a highly dynamic role during chondrocyte differentiation. Although required early in prechondrogenic cells, β-catenin activity is downregulated as chondrocytes begin differentiation, becoming active again at late stages of chondrocyte hypertrophy to promote osteoblast differentiation and mineralization (Ben-Ze'ev and Geiger, 1998; Day et al., 2005; Hartmann and Tabin, 2000; Hill et al., 2005; Hwang et al., 2005; Ryu et al., 2002; Willert and Nusse, 1998). Abnormally high or low levels of β-catenin at inappropriate stages of chondrogenesis are inhibitory to differentiation and can cause abnormal hypertrophy, chondrocyte disorganization, stimulation of osteoblast differentiation and premature mineralization (Day et al., 2005; Hartmann and Tabin, 2000; Hill et al., 2005; Hwang et al., 2005; Ryu et al., 2002; Willert and Nusse, 1998). Although the processes governing cranial NCC-derived chondrocyte differentiation during craniofacial development have been well characterized, the upstream mechanisms driving spatial and temporal activation and repression of GRNs and signaling pathways, in particular canonical Wnt/β-catenin, remain largely unknown.

Several chromatin modifiers have important regulatory roles in cranial NCC and craniofacial development (Liu and Xiao, 2011). Among these are the PRDM (positive regulatory domain) family of lysine methyltransferases, which control gene expression by epigenetic modulation of chromatin accessibility, directly binding DNA via zinc-finger domains, or interacting with other protein complexes (Di Zazzo et al., 2013; Fog et al., 2012; Hohenauer and Moore, 2012). Human genome-wide association studies have associated single nucleotide polymorphisms in the genes encoding two of these PRDMs, PRDM3 (EVI1/MECOM) and PRDM16, with craniofacial abnormalities, including cleft lip/palate and variation in facial morphology (Jugessur et al., 2010; Shaffer et al., 2016; Li et al., 2019; Liu et al., 2012; White et al., 2021).

PRDM3 and PRDM16 are important in a variety of developmental processes in mouse and zebrafish, acting as both direct and indirect repressors or activators of specific GRNs depending on the cellular context (Baizabal et al., 2018; Bjork et al., 2010; Ding et al., 2013; Harms et al., 2015; Kajimura et al., 2009, 2008; Seale et al., 2008, 2007; Warner et al., 2007; Arai et al., 2011; Goyama and Kurokawa, 2010; Goyama et al., 2008; Sato et al., 2008). Although some genetic compensation exists between these two paralogs with their high amino acid sequence homology and similar developmental expression patterns, there is also evidence suggesting that they have independent functions (Shull et al., 2020). Both *Prdm3* and *Prdm16* are necessary for craniofacial

[1]Department of Craniofacial Biology, University of Colorado Anschutz Medical Campus, Aurora, CO 80045, USA. [2]Department of Pharmacology and University of Colorado Cancer Center, University of Colorado Anschutz Medical Campus, Aurora, CO 80045, USA. [3]Division of Cellular Therapy, The University of Tokyo, Tokyo, 108-8639, Japan. [4]Department of Hematology and Oncology, The University of Tokyo, Tokyo, 113-8655, Japan. [5]Department of Pediatrics, University of Colorado Anschutz Medical Campus, Aurora, CO 80045, USA.
*Present address: Department of Cell Biology, University of Oklahoma Health Sciences Center, Oklahoma City, OK 73104, USA. ‡Present address: Department of Immunotherapy and Precision Immuno-Oncology, Cleveland Clinic, Cleveland, OH 44195, USA.

§Author for correspondence (Kristin.Artinger@cuanschutz.edu)

L.C.S., 0000-0001-7537-8516; E.S.L., 0000-0001-6795-0260; J.C.C., 0000-0003-3158-9682; K.B.A., 0000-0002-3003-6042

Handling Editor: Liz Robertson
Received 6 August 2021; Accepted 13 January 2022

Development (2022) 149, dev200082. doi:10.1242/dev.200082

skeletal development (Ding et al., 2013; Shull et al., 2020), yet the exact mechanism(s) involved in mediating cranial NCC-derived cartilage differentiation and craniofacial development are unknown.

In this study, we utilized zebrafish and mouse genetic models to dissect the molecular functions of Prdm3 and Prdm16 in chondrogenesis during craniofacial development. Based on our data, we hypothesize that Prdm3 acts as a transcriptional repressor whereas Prdm16 serves as an activator of gene expression to balance canonical Wnt/β-catenin transcriptional activity during chondrocyte differentiation. In doing so, Prdm3 and Prdm16 control proper spatial and temporal development of the vertebrate craniofacial skeleton.

RESULTS

prdm3 and *prdm16* are required for craniofacial chondrocyte stacking and polarity

Previous studies have shown that loss of either *prdm3* or *prdm16* causes moderate overall craniofacial phenotypes, namely mild hypoplasia, in the developing zebrafish pharyngeal skeleton (Shull et al., 2020). We confirmed these observations by assessing the cartilage and bone phenotypes of *prdm3* and *prdm16* mutant 6-day-old zebrafish larvae (Fig. 1A-C′). However, high magnification of the hypoplastic cartilage elements within the craniofacial skeleton revealed significant abnormal chondrocyte organization (Fig. 1D). Unlike the stacked chondrocytes of wild-type larvae, chondrocytes in *prdm3*$^{-/-}$ and *prdm16*$^{-/-}$ mutants were highly disorganized. This was quantified by measuring the angle between adjacent chondrocytes in the direction of growth of that cartilage element (Fig. 1E,F). The more organized the cells, the closer the angle between adjacent cells to 180°. Loss of *prdm3* and *prdm16* caused a significant (33.4% and 34.6%, respectively) reduction of this angle (Fig. 1F). The number of cells per unit of area within these cartilage structures was increased in both *prdm3*$^{-/-}$ (∼32.3%) and *prdm16*$^{-/-}$ (∼29.6%) mutants (Fig. 1G). Previous work has demonstrated that outgrowth of pre-cartilaginous condensations requires cell-cell intercalations and changes in cell shape (hypertrophy) rather than extensive proliferation (Kimmel et al., 2010, 1998; Le Pabic et al., 2014). Loss of *prdm3* and *prdm16* causes no change in proliferation during early development of cartilage structures (Shull et al., 2020). As such, the increased number of cells per tissue area observed in *prdm3* and *prdm16* mutants likely results from the failure of these chondrocytes to intercalate properly and their inability to expand their cell shape for growth. To evaluate changes in cell intercalation and extension, live imaging from 56 hours post-fertilization (hpf) to 72 hpf was performed on wild-type, *prdm3*$^{-/-}$ and *prdm16*$^{-/-}$ zebrafish larvae crossed into the *Tg(−4.9sox10:EGFP)* (Carney et al., 2006) transgenic background. Live imaging revealed failure of the chondrocytes within cartilage structures to extend during development in both *prdm3* and *prdm16* mutants (Movies 1-3, Fig. S1A-C) and suggested that chondrocyte cell polarity was also abrogated in *prdm3* and *prdm16* mutants.

To assess changes in cell polarity, wild-type, *prdm3*$^{-/-}$ or *prdm16*$^{-/-}$ larvae were stained with acetylated α-tubulin to label microtubule-organizing centers (MTOCs) at 75 hpf, a time point at which chondrocyte cell-cell rearrangements and polarity have stabilized, and cells are oriented in a specific direction for growth. MTOCs in pre-chondrocytes are oriented towards the center of each condensation of the cartilage element. Over time, these cells re-orient themselves in a uniform manner along dorsal-ventral axes (Le Pabic et al., 2014). At 75 hpf, the MTOCs in the chondrocytes of the palatoquadrate in wild-type larvae were stable and localized ventrally toward the Meckel's cartilage and the jaw joint (Fig. 1H,H′, Fig. S2A-A‴). However, the MTOCs in stage-matched *prdm3*$^{-/-}$ (Fig. 1I,I′, Fig. S2B-B‴) and *prdm16*$^{-/-}$ (Fig. 1J,J′, Fig. S2C-C‴) failed to rearrange and orient themselves uniformly along this ventral axis and instead were positioned dorsally, or towards the center of the original condensation (Fig. 1I-J′, Fig. S2B-C‴). Quantification of MTOC orientation in wild-type palatoquadrates showed that 65% of chondrocytes at this stage were ventrally polarized, as denoted by MTOC puncta positioned directionally at the 180° quadrant of the cell (Fig. 1K,L,O). Conversely, loss of *prdm3* and *prdm16* caused a significant reduction (∼25%) in the percentage of uniformly ventrally oriented chondrocytes (180°), which corresponded to an increase in the number of chondrocytes that were instead positioned dorsally (0°) or towards the center of the cartilage element (90° or 270°) (Fig. 1M-O). These results demonstrate *Prdm3* and *Prdm16* are important for facilitating proper chondrocyte differentiation, including orientation, intercalation and organization in the cartilage elements that form during craniofacial cartilage morphogenesis.

Neural crest-specific function of *Prdm3* and *Prdm16* is required for chondrocyte organization in Meckel's cartilage of the developing murine mandible

Prdm3 and Prdm16 are expressed in the facial prominences during murine development (Fig. S3A-B′) and we have recently shown that Prdm3 and Prdm16 share some conserved functions across vertebrate species (Shull et al., 2020). To determine whether changes in craniofacial chondrocyte development were conserved in mammals with loss of *Prdm3* and *Prdm16*, we conditionally ablated *Prdm3* and *Prdm16* in the murine neural crest lineage using the *Wnt1-Cre* driver (Chai et al., 2000; Danielian et al., 1998). Both homozygous *Prdm3*$^{fl/fl}$;*Wnt1-Cre*$^{+/Tg}$ and *Prdm16*$^{fl/fl}$;*Wnt1-Cre*$^{+/Tg}$ mutant animals were born at Mendelian ratios and survived to embryonic day (E) 18.5. Viability of mutant embryos past E18.5 was not assessed, but we predict that neither mutant would survive postnatally owing to either defects in heart development (*Prdm3*) or failure to thrive due to cleft palate defects (*Prdm16*) (Goyama et al., 2008; Hoyt et al., 1997; Bjork et al., 2010; Shull et al., 2020; Warner et al., 2013). Homozygous *Prdm3* mutant animals developed a subtle craniofacial phenotype, namely mild anterior mandibular hypoplasia and slight defects in snout extension (Fig. 2B-B″,E). Homozygous *Prdm16*$^{fl/fl}$;*Wnt1-Cre*$^{+/Tg}$ mutants presented with a variety of craniofacial defects, similar to those observed with loss of *Prdm16* in the early epiblast, suggesting a cell-autonomous function in the neural crest (Bjork et al., 2010; Shull et al., 2020). Abnormalities included snout extension defects, anterior mandibular hypoplasia, secondary cleft palate and middle ear defects with severe hypoplasia of the tympanic rings, incus, malleus and retroarticular process of the squamosal bone (Fig. 2C-C″,E, Fig. S3C-H″).

The shared phenotype in both mutants was mandibular hypoplasia (Fig. 2A-E). Alcian Blue- and Alizarin Red-stained skeletal preparations confirmed anterior mandibular hypoplasia (Fig. 2A′-C″), which was quantified by measuring the ratio of the anterior portion of the mandible relative to the posterior length (Fig. 2D,E). This phenotype parallels some of the hypoplasia seen in *prdm3* and *prdm16* zebrafish mutants and suggests changes to the cellular development and maturation of the chondrocytes in cartilaginous structures (Meckel's cartilage) that support the formation of the mandible. To assess chondrocytes within the Meckel's cartilage histologically, sagittal sections were collected from control, *Prdm3*$^{fl/fl}$;*Wnt1-Cre*$^{+/Tg}$ and *Prdm16*$^{fl/fl}$;*Wnt1-Cre*$^{+/Tg}$ at E14.5, the stage of cartilage development at which the chondrocytes have undergone rapid growth and are starting to undergo pre-hypertrophy (Fig. 2F-H″). Safranin O and Fast Green

Development (2022) 149, dev200082. doi:10.1242/dev.200082

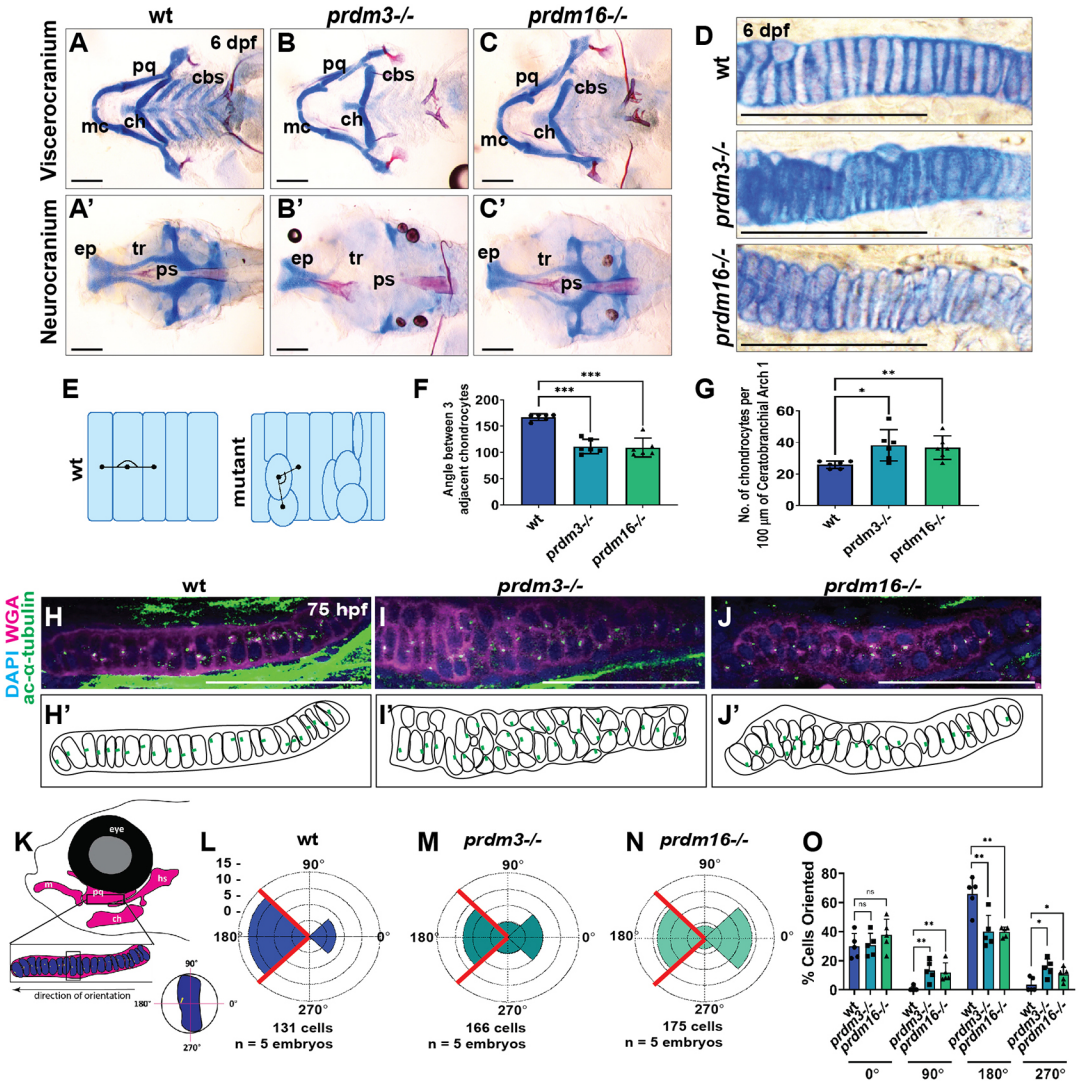

Fig. 1. *prdm3* and *prdm16* are necessary for chondrocyte stacking and polarity in the zebrafish craniofacial skeleton. (A-G) Wild-type (wt), *prdm3*$^{-/-}$ and *prdm16*$^{-/-}$ zebrafish embryos were collected at 6 dpf and stained with Alcian Blue and Alizarin Red. (A-D) Images of dissected and flat-mounted viscerocranium (A-C) and neurocranium (A′-C′), and high magnification of chondrocytes (D). cbs, ceratobranchials; ch, ceratohyal; ep, ethmoid plate; mc, Meckel's cartilage; pq, palatoquadrate; ps, parasphenoid; tr, trabeculae. Scale bars: 100 µm. (E,F) Quantification of chondrocyte organization (F) as schematized in E (*n*=6 per genotype); mean±s.d. Black lines in E indicate angle measurement between adjacent chondrocytes. (G) Quantification of the number of chondrocytes per 100 µm of tissue (*n*=6 per genotype); mean±s.d. (H-O) Wild-type, *prdm3*$^{-/-}$ or *prdm16*$^{-/-}$ larvae were immunostained with acetylated α-tubulin to label MTOCs, denoting directional growth, and counterstained with DAPI and wheat germ agglutinin (WGA) at 75 hpf (H-J). Shown are lateral high-magnification views of the palatoquadrate. Scale bars: 50 µm. (H′-J′) Schematics showing misoriented chondrocytes. Green dots represent the localization of acetylated α-tubulin puncta. (K-O) Quantification of chondrocyte polarity (positioning of acetylated α-tubulin puncta), as depicted in K for wild type (L), *prdm3*$^{-/-}$ (M) and *prdm16*$^{-/-}$ (N). (O) Percentage of cells in each indicated quadrant normalized to the total number of cells for each genotype. (*n*=5 per genotype); mean±s.d. *$P \leq 0.05$, **$P \leq 0.005$, ***$P \leq 0.001$; ns, not significant (unpaired, two-tailed Student's *t*-test).

staining of sections revealed changes to the chondrocyte organization and morphology in mutant animals compared with controls. In controls, chondrocytes were starting to swell and become pre-hypertrophic as evidenced by expansion of the intracellular space (Fig. 2F′,F″). These cells were also organized into stacks extending from the top of the cartilage structure to the bottom of the Meckel's cartilage (Fig. 2F′,F″). By contrast, *Prdm3* mutant chondrocytes were smaller and tightly packed, suggesting a stall in their maturation process (Fig. 2G′,G″). *Prdm16* mutant chondrocytes were unsynchronized; some appeared compacted like those in the *Prdm3* mutants whereas others seemed to be undergoing accelerated pre-hypertrophy (Fig. 2H′,H″). In both mutants, the chondrocytes were disorganized (Fig. 2G″,H″).

Quantification of chondrocyte cell area and the number of cells per tissue area supported these observations of cellular changes. Loss of *Prdm3* led to a significant ∼22% decrease in chondrocyte cell area (Fig. 2I) and a corresponding ∼16% increase of total number of cells per tissue area (Fig. 2J). Decreased cell area was near significance (P=0.0658), but there were no significant changes in the total number of cells with loss of *Prdm16*, likely because of the heterogeneric differentiation state of chondrocytes observed in these animals (Fig. 2I,J). The cellular changes observed in the developing Meckel's cartilage with loss of *Prdm3* and *Prdm16* suggest altered chondrocyte differentiation, which likely contributes to the anterior mandibular hypoplasia observed in these mutants. Importantly, chondrocytes within both zebrafish and mouse

Development (2022) 149, dev200082. doi:10.1242/dev.200082

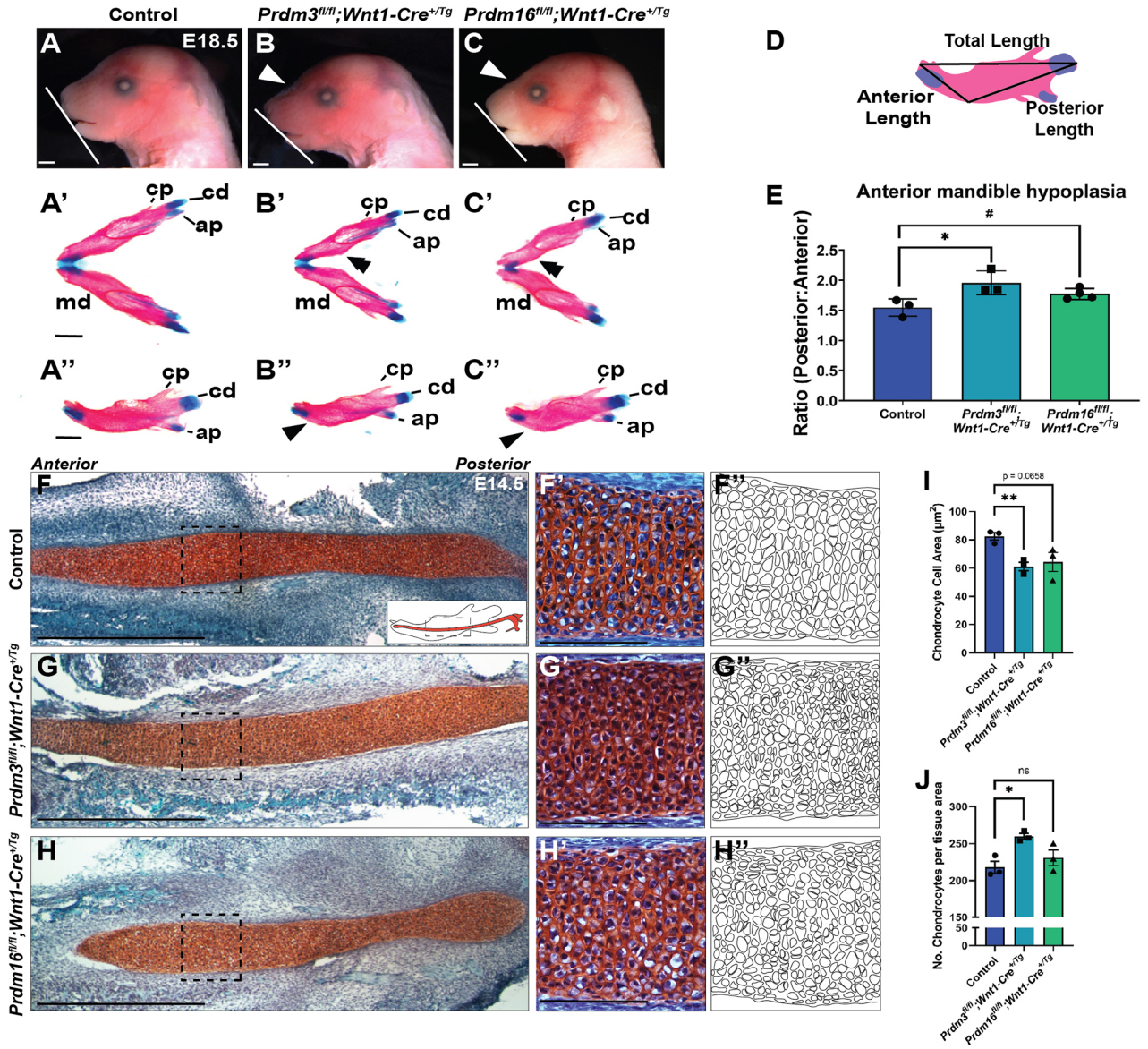

Fig. 2. Neural crest-specific function of *Prdm3* and *Prdm16* is required for chondrocyte organization in the Meckel's cartilage of the developing murine mandible. (A-J) *Prdm3*$^{fl/fl}$ or *Prdm16*$^{fl/fl}$ female mice were bred to *Prdm3*$^{fl/+}$;*Wnt1-Cre*$^{+/Tg}$ or *Prdm16*$^{fl/+}$;*Wnt1-Cre*$^{+/Tg}$ males and embryos were collected at the indicated time points. (A-C) Lateral images of the head show snout defects (white arrowheads) and mandible hypoplasia (white lines) in *Prdm3* and *Prdm16* mutants. (A′-C′) Alcian Blue- and Alizarin Red-stained mandibles were dissected from control or mutant animals. (A″-C″) Lateral views of the right half of the mandible. ap, angular process; cd, condylar process; cp, coronoid process; md, mandible. Black arrowheads and double arrowheads denote morphological irregularities in the mandible. (D,E) Quantification of anterior mandibular hypoplasia (ratio between the length of the anterior and posterior portions of the mandible; E) as schematized in D (n=3 per genotype); mean±s.d. (F-H) Safranin O- and Fast Green-stained sagittal sections of the Meckel's cartilage at E14.5 in control (F), *Prdm3* (G) or *Prdm16* (H) mutants. Scale bars: 100 µm. (F′-H′) High-magnification images of the chondrocytes from the boxed regions in F-H. Scale bars: 100 µm. (F″-H″) Schematics showing chondrocyte cell shapes. (I,J) Quantification of chondrocyte cell area (I) and cell number per tissue area (J) (n=3 per genotype); mean±s.d. *P≤0.05, **P≤0.005, $^{\#}P$<0.1; ns, not significant (unpaired, two-tailed Student's t-test).

craniofacial structures were abnormal with loss of *Prdm3* and *Prdm16*, suggesting a conserved function of these factors in regulation of chondrocyte differentiation and maturation in vertebrate craniofacial cartilage development.

prdm3 and *prdm16* regulate global gene expression in cranial neural crest cells

To dissect the molecular mechanisms of *prdm3* and *prdm16* in controlling cranial NCC cartilage derivative differentiation, we analyzed the transcriptome of zebrafish cranial NCCs. Each mutant line was crossed into the *Tg(−4.9sox10:EGFP)* background (Carney et al., 2006). *sox10:EGFP*-positive cranial NCCs were isolated from wild-type, *prdm3*$^{-/-}$ and *prdm16*$^{-/-}$ embryos at 48 hpf by fluorescence-activated cell sorting (FACS) and subjected to RNA sequencing (RNA-seq). Transcriptomic analysis revealed striking differences in overall gene expression with loss of *prdm3* or *prdm16* (Fig. 3). In *prdm3*$^{-/-}$ mutants, an overwhelming 2688 genes were significantly upregulated, but only 189 genes were significantly downregulated (Fig. 3A,B). Conversely, in *prdm16* mutants the majority of differentially expressed genes were significantly downregulated (1370), and only 279 were significantly upregulated (Fig. 3A,D). Gene ontology (GO)

Development (2022) 149, dev200082. doi:10.1242/dev.200082

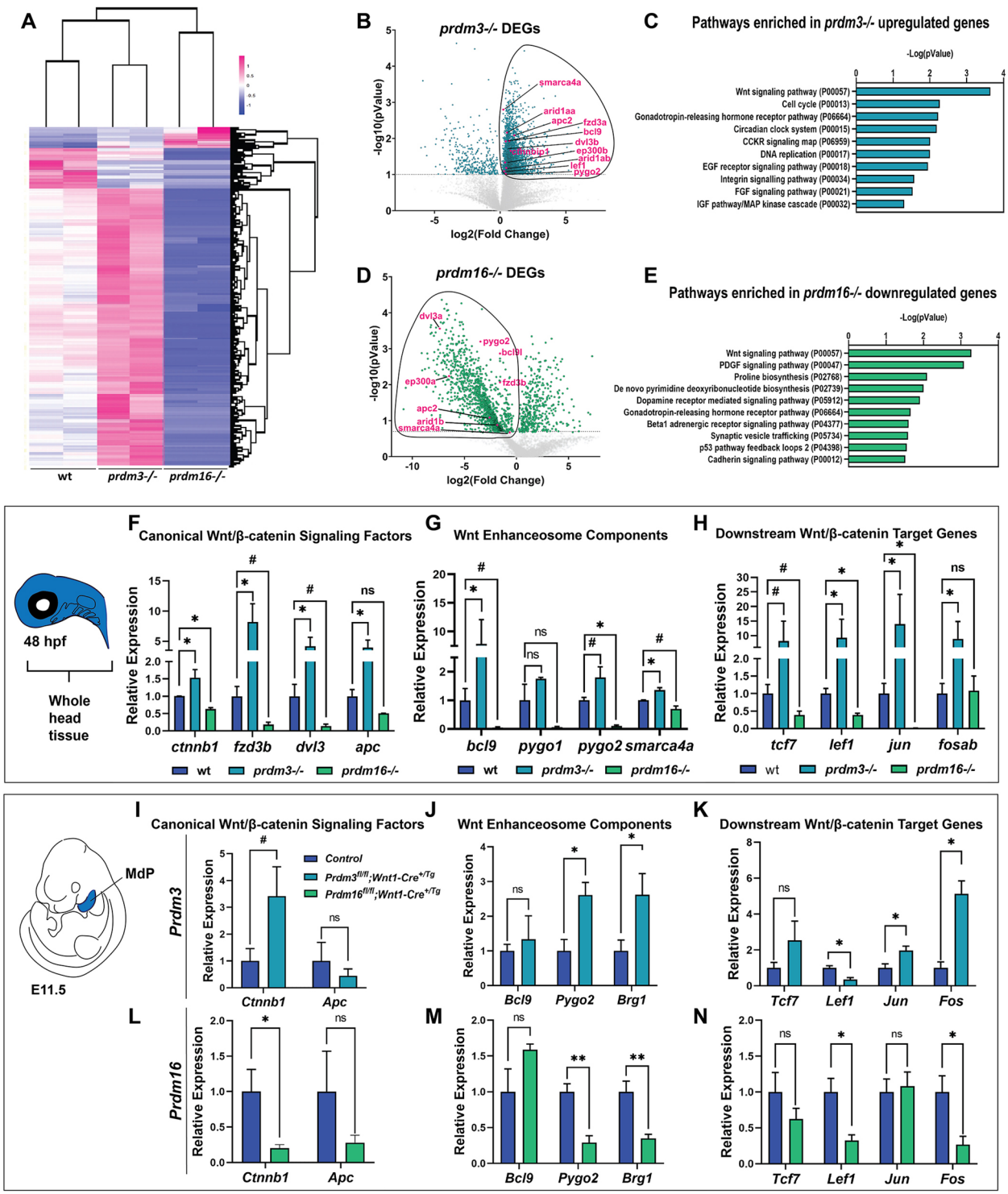

Fig. 3. Prdm3 and Prdm16 differentially regulate Wnt/β-catenin signaling components in cranial NCCs. (A-E) RNA-seq was performed on *sox10:EGFP* FACS-sorted cranial NCCs at 48 hpf from wild-type, *prdm3*$^{-/-}$ and *prdm16*$^{-/-}$ zebrafish. (A) Heatmap showing z-scaled FPKM values for significant genes from *prdm3*$^{-/-}$ and *prdm16*$^{-/-}$ mutants. (B,D) Volcano plots showing the distribution of DEGs in *prdm3*$^{-/-}$ (B) and *prdm16*$^{-/-}$ (D), including Wnt/β-catenin signaling components (highlighted in magenta). (C,E) The upregulated genes in *prdm3* mutants and downregulated genes in *prdm16* mutants (circled in B and D) were subjected to GO (PANTHER) Pathway Enrichment Analysis. (F-H) Validation of RNA-seq transcriptomic changes on RNA isolated from whole heads pooled from five to seven embryos per genotype; mean±s.d. RT-qPCR was performed for selected Wnt/β-catenin signaling component genes, including canonical Wnt/β-catenin signaling factors (*ctnnb1*, *fzd3b*, *dvl3*, *apc*) (F); Wnt enhanceosome transcriptional complex members (*bcl9*, *pygo1*, *pygo2*, *smarca4a*) (G); and downstream Wnt/β-catenin target genes (*tcf7*, *lef1*, *jun*, *fosab*) (H). (I-N) Validation of zebrafish RNA-seq transcriptomic changes in E11.5 mouse mandibular processes. RT-qPCR was performed for selected genes, including canonical Wnt/β-catenin signaling factors (*Ctnnb1*, *Apc*) in *Prdm3* (I) and *Prdm16* (L) mutants; Wnt enhanceosome transcriptional complex members [*Bcl9*, *Pygo2*, *Brg1* (*Smarca4a*)] in *Prdm3* (J) and *Prdm16* (M) animals; and downstream Wnt/β-catenin target genes (*Tcf7*, *Lef1*, *Jun*, *Fos*) in *Prdm3* (K) and *Prdm16* (N) mutants. *n*=3 per genotype; mean±s.d. MdP, mandibular process. **P*≤0.05, ***P*≤0.005, $^{\#}P$≤0.1; ns, not significant (unpaired, two-tailed Student's *t*-test).

Development (2022) 149, dev200082. doi:10.1242/dev.200082

pathway analysis was performed separately on the genes that were upregulated in *prdm3* mutants and those downregulated in *prdm16* mutants. Canonical Wnt/β-catenin was identified as the top signaling pathway enriched in both the upregulated genes in *prdm3* mutants and the downregulated genes in *prdm16* mutants (Fig. 3B-E, Fig. S4). The opposing differentially expressed genes belonging to the canonical Wnt/β-catenin signaling axis included *ctnnb1* and other signal transducers (Fzd gene family, Dvl gene family, *apc*) as well as downstream Wnt/β-catenin transcriptional targets (*fosab*, *jun*, *tcf7*, *lef1*) (Fig. 3B,D, Fig. S4C,D). Many of these genes encoded factors involved in the assembly of the Wnt/β-catenin enhanceosome transcriptional complex [*bcl9/bcl9l*, *pygo1/2*, *smarca4a* (also known as *brg1*), *ep300a/b*, *arid1aa/ab*, *tcf7*, *lef1*] (Fig. 3B,D, Fig. S4C,D). These opposing transcriptomic profiles in *prdm3*$^{-/-}$ and *prdm16*$^{-/-}$ mutants were validated by real-time quantitative polymerase chain reaction (RT-qPCR) on RNA from whole heads of wild-type, *prdm3*$^{-/-}$ or *prdm16*$^{-/-}$ embryos at 48 hpf (Fig. 3F-H). The trends of gene expression of canonical Wnt pathway genes (*ctnnb1*, *fzd3b*, *dvl3*, *apc*) (Fig. 3F), components of the Wnt-enhanceosome transcriptional complex (*bcl9*, *pygo1/2*, *smarca4a*) (Fig. 3G) and downstream Wnt/β-catenin target genes (*tcf7*, *lef1*, *jun*, *fosab*) (Fig. 3H), followed the same pattern: elevated expression with loss of *prdm3* and, conversely, decreased expression with loss of *prdm16*.

To determine whether changes to the expression of Wnt/β-catenin signaling components identified by RNA-seq in zebrafish were also differentially expressed during formation of the mouse Meckel's cartilage, RNA was extracted from the mesenchyme of the mandibular processes of pharyngeal arch 1 at E11.5 from control, *Prdm3*$^{fl/fl}$*;Wnt1-Cre*$^{+/Tg}$ and *Prdm16*$^{fl/fl}$*;Wnt1-Cre*$^{+/Tg}$ embryos and RT-qPCR was performed for Wnt/β-catenin signaling components (Fig. 3I-N). Consistent with the zebrafish differential expression, loss of *Prdm3* in developing murine mandibular facial tissue led to an increase in *Ctnnb1* (Fig. 3I) expression, as well as members of the Wnt enhanceosome (*Bcl9*, *Pygo2*, *Brg1*) (Fig. 3J) and subsequent downstream Wnt/β-catenin target genes (*Tcf7*, *Jun*, *Fos*) (Fig. 3K), whereas loss of *Prdm16* caused decreased expression of these factors (Fig. 3L-N). Although there were some differences in expression between species (i.e. decreased *Apc* and *Lef1* expression in *Prdm3* mutant mouse tissues, in contrast to elevated expression in zebrafish), the overall trends were similar and suggest that Prdm3 and Prdm16 exert opposing effects to balance Wnt/β-catenin signaling component gene expression and that this process is conserved across tetrapods and teleosts.

prdm3 and *prdm16* control β-catenin stabilization and localization in craniofacial chondrocytes

Given that canonical Wnt/β-catenin signaling was the most differentially altered pathway in both *prdm3* and *prdm16* mutant zebrafish, and many of the differentially expressed genes associated with Wnt/β-catenin signaling were those involved in the formation of the Wnt/β-catenin enhanceosome transcriptional complex and retention of nuclear β-catenin, we next assessed changes in active β-catenin localization. Whole-mount immunofluorescence for nuclear β-catenin (phosphorylated tyrosine residue 489) was performed on wild-type, *prdm3*$^{-/-}$ or *prdm16*$^{-/-}$ zebrafish larvae at 75 hpf. Unlike wild-type chondrocytes, which have low abundance of nuclear β-catenin at this stage (Fig. 4A,D, Fig. S5A-A‴), *prdm3*$^{-/-}$ had a significant increase in the presence of nuclear β-catenin (Fig. 4B,D, Fig. S5B-B‴). Conversely, *prdm16*$^{-/-}$ had a dramatic reduction in the accumulation of nuclear β-catenin to levels significantly below that of wild-type chondrocytes (Fig. 4C,D, Fig. S5C-C‴).

To understand further canonical Wnt/β-catenin signaling in chondrocyte development in the craniofacial skeleton with loss of *prdm3* and *prdm16*, *prdm3*$^{-/-}$ and *prdm16*$^{-/-}$ zebrafish mutants were crossed into the Wnt reporter line *Tg(7xTCF-Xla.Sia:NLS-mCherry)*^{ia5Tg} (Moro et al., 2012) in combination with the *Tg(fli1:EGFP)* line (Lawson and Weinstein, 2002) to visualize Wnt-responsive cells in the pharyngeal arches and developing

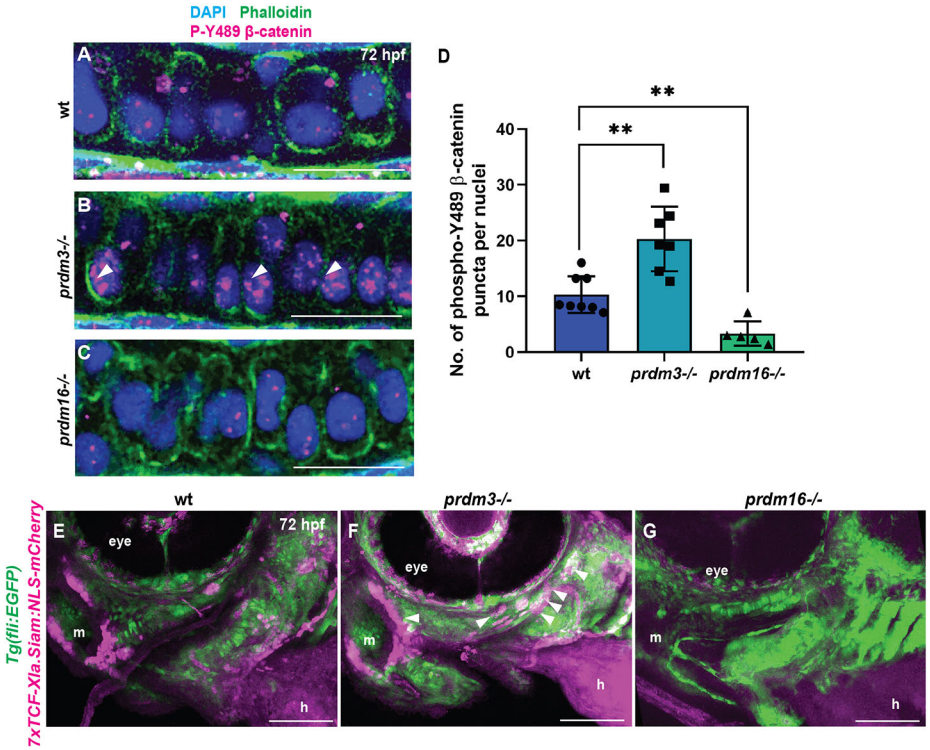

Fig. 4. Prdm3 and Prdm16 control β-catenin stabilization and localization in craniofacial chondrocytes. (A-D) Wild-type (wt), *prdm3*$^{-/-}$ and *prdm16*$^{-/-}$ zebrafish embryos were collected at 75 hpf and immunostained for nuclear β-catenin (phosphorylated tyrosine 489) and counterstained with phalloidin and DAPI (A-C). Shown are high-magnification lateral images of the palatoquadrate. Increased nuclear β-catenin (magenta) was observed in *prdm3*$^{-/-}$ (white arrowheads in B), which was significantly reduced in *prdm16*$^{-/-}$ (C). (D) Quantification of the number of β-catenin puncta across ten nuclei per individual and averaged across at least five embryos per genotype; mean±s.d. Scale bars: 50 µm. (E-G) *prdm3*$^{-/-}$ and *prdm16*$^{-/-}$ mutant lines were crossed into the Wnt reporter line *Tg(7xTCF-Xla.Siam:NLS-mCherry)* to assess Wnt-responsive cells. Shown are representative lateral-ventral views of 75 hpf wild-type (E), *prdm3*$^{-/-}$ (F) and *prdm16*$^{-/-}$ (G) embryos. Increased Wnt-responsive cells were identified in the pharyngeal arch tissues of *prdm3*$^{-/-}$ (F) (white arrowheads), with a dramatic decrease in Wnt-responsive cells in *prdm16*$^{-/-}$ (G) mutants compared with wild type (E). h, heart; m, mouth. Scale bars: 100 µm. **$P \leq 0.005$ (unpaired, two-tailed Student's *t*-test).

Development (2022) 149, dev200082. doi:10.1242/dev.200082

craniofacial cartilage elements (Fig. 4E-G). At 72 hpf, *prdm3* mutants had increased Wnt-responsive cells in the pharyngeal arch/craniofacial elements and other structures, including the heart, otic vesicle and perichondrium (Fig. 4F, Fig. S5E-E″). Conversely, few or no Wnt-responsive cells were present in *prdm16*$^{-/-}$ larvae (Fig. 4G, Fig. S5F-F″). Together, these results validate the transcriptional changes observed in both *prdm3* and *prdm16* mutants and correlate with differences in expression of factors (i.e. *bcl9*) involved in retaining β-catenin in the nucleus, assembling the Wnt enhanceosome and driving transcription of downstream target genes. Abnormal accumulation of nuclear β-catenin in *prdm3* mutant chondrocytes at later stages of chondrocyte development may explain the chondrocyte polarity, orientation, intercalation and differentiation defects, as high sustained β-catenin signaling can be inhibitory to cartilage differentiation (Hill et al., 2005; Hwang et al., 2005; Ryu et al., 2002; Sun et al., 2020). However, *prdm16* mutants have the same chondrocyte differentiation defects, but instead with reduced canonical Wnt/β-catenin signaling, suggesting that low maintenance levels of nuclear β-catenin activity may be required to help facilitate chondrocyte differentiation and maturation.

prdm3 and *prdm16* alter chromatin accessibility at *cis*-regulatory regions of Wnt/β-catenin signaling components in cranial NCCs

Previous work has implicated both Prdm3 and Prdm16 in the regulation of gene expression through methylation of lysine residues on histone H3: H3K9, a mark of repression, and H3K4, a mark associated with gene activation. Both H3K9me3 and H3K4me3 are significantly reduced in both *prdm3* and *prdm16* mutant zebrafish (Shull et al., 2020), suggesting global changes to the chromatin landscape. To understand how Prdm3 and Prdm16 are epigenetically regulating gene expression, specifically of canonical Wnt/β-catenin pathway components, assays for transposase-accessible chromatin paired with sequencing (ATAC-seq) were performed on FACS-sorted *sox10:EGFP* cranial NCCs isolated from pooled *prdm3* wild-type/heterozygotes (hets), *prdm3*$^{-/-}$, *prdm16* wild-type/hets, and *prdm16*$^{-/-}$ embryos at 48 hpf (Fig. 5).

prdm3 mutant embryos exhibited a noticeable increase in open chromatin compared with matched wild-type/het samples (Fig. 5A,B, Fig. S6A,B). To quantify differences in open chromatin state, we used DiffBind to measure read depth on a union peakset generated from peaks called by Genrich in the *prdm3* mutant and wild-type/het samples (Fig. 5E-G). This analysis identified 7870 peaks in the *prdm3*$^{-/-}$ embryos compared with 146 differential peaks identified from wild-type/het control siblings (Fig. 5E); 4917 regions were identified in both the *prdm3*$^{-/-}$ and wild-type/het samples (Fig. 5E). Significantly different differential peaks exhibited greater read depth in the *prdm3* mutant samples compared with their wild-type controls (Fig. 5F). This result is illustrated by the greater number of statistically significant differential ATAC peaks in *prdm3*$^{-/-}$ mutants (Fig. 5G; note that volcano plot is shifted with more peaks having greater depth in the *prdm3* mutant). We interpret these data to reflect a greater amount of open chromatin in the *prdm3* mutants at a genome-wide scale.

In contrast, loss of *prdm16* resulted in a slight decrease in open chromatin compared with matched wild-type/het samples (Fig. 5C,D, Fig. S6C,D). DiffBind analyses for *prdm16* mutants identified only 702 differential peaks in *prdm16*$^{-/-}$ embryos compared with 972 in the wild-type/het controls with an overlap of 4079 peaks across both genotypes (Fig. 5H). Although few peaks reached statistical significance in the Prdm16 comparison, we note that all differential peaks do exhibit a slight decrease in the average read depth in the *prdm16* mutants (Fig. 5I,J). Thus, we found an overall trend whereby read depth at ATAC peaks was generally lower in the *prdm16* mutants compared with wild-type/het control samples, even if most peaks did not reach statistical significance. Importantly, this pattern is opposite to that observed for *prdm3* mutants, for which differential ATAC peaks often exhibited higher read depth in *prdm3* mutants (compare Venn diagrams and volcano plots in Fig. 5E-J).

ATAC peak regions with greater depth in the *prdm3*$^{-/-}$ mutants were largely associated with promoters and exons (Fig. 5K), in contrast to matched *prdm3* wild-type/het controls for which peak regions were instead largely located within intronic and intergenic regions (Fig. 5K). The relatively smaller number of ATAC peaks with greater depth in the *prdm16*$^{-/-}$ mutants were mostly associated with intergenic regions (Fig. 5L). Across both mutant comparisons, 380 shared peaks were identified with greater read depth across the two mutants compared with their respective controls. Thus, approximately half of the peaks with greater chromatin accessibility in the *prdm16* mutants (702 total) also had greater chromatin accessibility in the *prdm3* mutants.

We next used the footprinting pipeline TOBIAS (transcription factor occupancy prediction by investigation of ATAC-seq signal) (Bentsen et al., 2020) to predict transcription factor occupancy in regions exhibiting differential chromatin states in the *prdm3* and *prdm16* zebrafish mutants. For these analyses, we limited our peak sets to the set of unique peaks identified by Genrich for each genotype regardless of whether DiffBind identified read depth at a peak as statistically significant or not. Thus, for these analyses we used TOBIAS to search for enriched transcription factors predicted to be uniquely bound in either the *prdm3* or *prdm16* mutants relative to their wild-type/het controls.

For regions unique to *prdm3*$^{-/-}$ mutants, the top 10 transcription factor families with predicted increased occupancy based on motif enrichment were associated with genes necessary for cell growth, differentiation, and developmental patterning processes (Fig. 5M, Tables S1 and S2). Several of these transcription factors are activated downstream of Wnt signaling [Ovol1, Hes7 (Her1), Tead2 (Tead family), Gbx2] whereas others (Etv5, Arnt2) recruit protein complexes to modulate chromatin architecture or facilitate gene expression through enhancers (Fig. 5M). One of the top transcription factor families predicted to be differentially bound in *prdm3*$^{-/-}$ mutant cranial NCCs was Fos/Jun. Fos/Jun is a known transcriptional target of canonical Wnt/β-catenin signaling, and our RNA-seq identified Fos/Jun as differentially expressed at the transcriptional level in both *prdm3* and *prdm16* mutants (Fig. 3).

The top 10 transcription factors enriched in *prdm16*$^{-/-}$ cranial NCCs included several factors that are important in neural crest cell development (Tfap2b) and formation of complexes important for facilitating chromatin remodeling [Plagl1 (Plag family)]. In addition, one of the top factors included Pparg. Prdm16 is already known to interact with Pparg to regulate brown fat adipogenesis (Kajimura et al., 2009, 2008) (Fig. 5N, Table S3). Pparg and Wnt/β-catenin can antagonistically influence expression of each other: activated Pparg decreases Wnt/β-catenin and elevated Wnt/β-catenin inhibits Pparg (Davis and Zur Nieden, 2008; Moldes et al., 2003; Takada et al., 2010). This pattern of Wnt/β-catenin expression and occupancy of Pparg correlates with the decreased Wnt/β-catenin signature observed in *prdm16* mutants. Because most genes were downregulated and associated with less-accessible chromatin in *prdm16*$^{-/-}$, the transcription factors that had a predicted decrease in binding affinity in the mutants were also assessed (Fig. 5O, Table S4). One of the top transcription factors

Development (2022) 149, dev200082. doi:10.1242/dev.200082

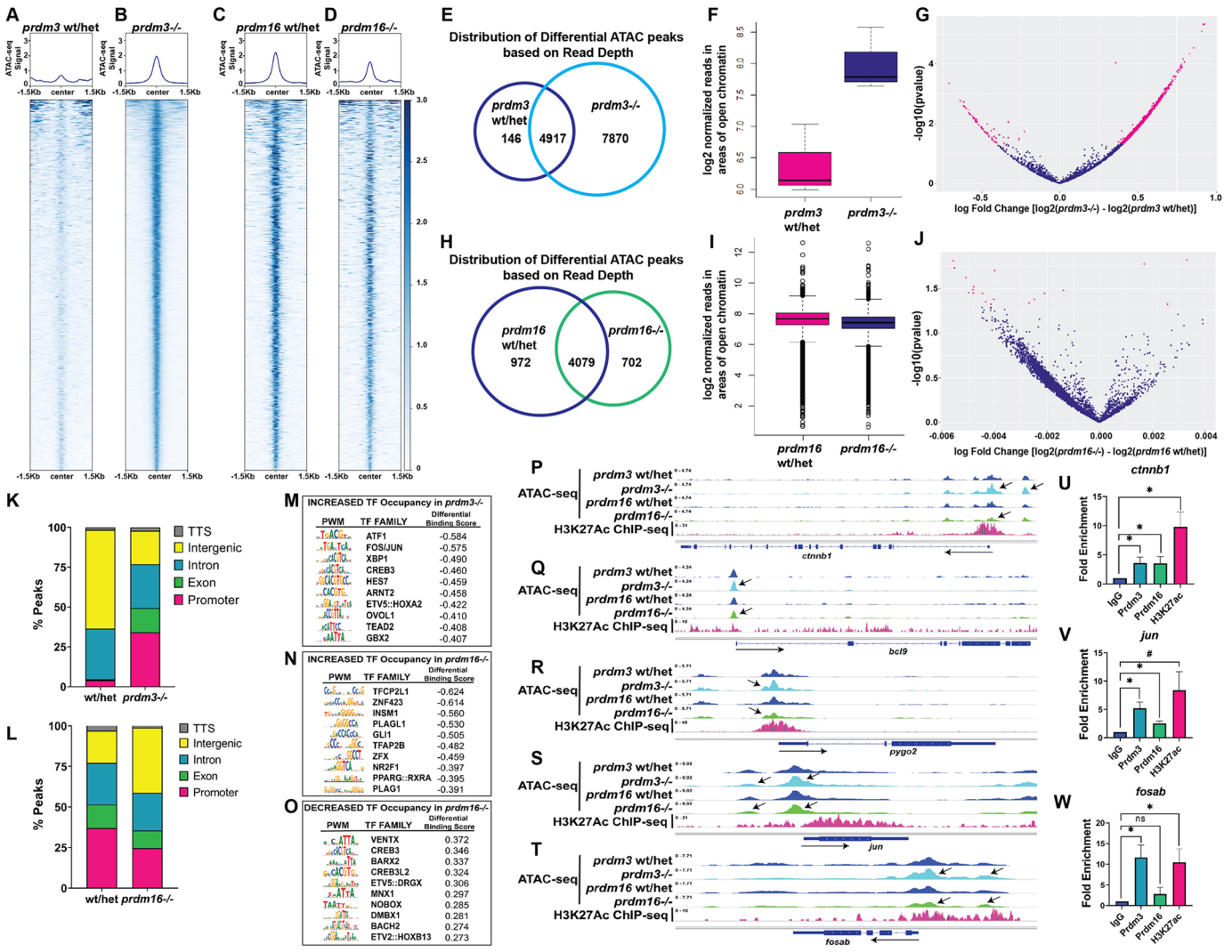

Fig. 5. Prdm3 and Prdm16 alter chromatin accessibility at *cis*-regulatory regions of Wnt/β-catenin signaling components in cranial NCCs. (A-T) ATAC-seq was performed on *sox10:EGFP* FACS-sorted cells from wild-type, *prdm3*$^{-/-}$ and *prdm16*$^{-/-}$ zebrafish at 48 hpf. (A-D) Coverage heatmaps depicting the differences 1.5 kb upstream and downstream of centered peaks across the genome in controls (A,C), *prdm3*$^{-/-}$ (B) and *prdm16*$^{-/-}$ (D) mutants. (E,H) Venn diagrams representing the unique and overlapping differential ATAC-seq peaks based on differences in read depth across two replicates from *prdm3*$^{-/-}$ (E) and *prdm16*$^{-/-}$ (H) relative to their corresponding control groups as determined by DiffBind analysis. (F,I) Box plots representing the distribution of normalized read depth concentrations across all significant differential ATAC regions in *prdm3*$^{-/-}$ (F) and all differential ATAC regions in *prdm16*$^{-/-}$. (I) compared with their respective controls. The interquartile range of the box extends from the 25th percentile to the 75th percentile with the line through the box representing the median. Whiskers extend to 1.5× the interquartile range with dots representing outliers. Derivation of these box plots was based a two-sided Wilcoxon Mann–Whitney test computed during DiffBind analysis. (G,J) Volcano plots showing distribution of differential ATAC peaks by fold change and significance in *prdm3*$^{-/-}$ (G) and *prdm16*$^{-/-}$ (J). Magenta dots represent those differential peaks meeting the threshold of $P \leq 0.05$. (K,L) Annotation of enriched peaks in *prdm3*$^{-/-}$ (K) and *prdm16*$^{-/-}$ (L). (M-O) Transcription factor occupancy prediction by investigation of ATAC-seq signal (T±) was performed on *prdm3* and *prdm16* mutant ATAC datasets. Shown are the top 10 transcription factors with predicted increased occupancy in *prdm3*$^{-/-}$ (M) and *prdm16*$^{-/-}$ (N) and decreased occupancy in *prdm16*$^{-/-}$ (O); $P \leq$E−20. Each table shows the position weight matrix (PWM) for each transcription factor (TF) motif, the transcription factor family, and the differential binding score. (P-T) Tracks showing the distribution of peaks (chromatin accessibility), compared with previously published H3K27ac ChIP-seq datasets (Bogdanovic et al., 2012) from 48 hpf whole embryos, at specific Wnt/β-catenin signaling component target genes that were differentially expressed in *prdm3* and *prdm16* mutants: *ctnnb1* (P), *bcl9* (Q), *pygo2* (R), *jun* (S) and *fosab* (T). (U-W) CUT&RUN paired with RT-qPCR was performed on 48 hpf whole zebrafish embryos with antibodies directed toward Prdm3, Prdm16 and H3K27ac. Enrichment (normalized to IgG) was assessed with primers flanking putative Prdm3- and Prdm16-binding sites near promoter regions (within 1000 bp of the TSS) of *ctnnb1* (U), *jun* (V) and *fosab* (W). CUT&RUN-RT-qPCR experiments were performed three times; mean±s.d. is shown. $^{*}P \leq 0.05$, $^{\#}P \leq 0.1$; ns, not significant (unpaired, two-tailed Student's *t*-test).

with significantly decreased occupancy was Barx2. Barx2 has important functions in regulating cell-cell adhesions and aggregations and plays a crucial role in craniofacial development and chondrogenesis (Jones et al., 1997; Meech et al., 2005).

Because Wnt/β-catenin signaling was the most differentially regulated pathway from our transcriptomic data, we next assessed changes in chromatin accessibility at differentially expressed Wnt/β-catenin signaling components and target genes (Fig. 5P-T, Fig. S6E-I). Consistent with our transcriptomic data, loss of *prdm3* led to increased open chromatin at canonical Wnt/β-catenin components, including *ctnnb1* (Fig. 5P), *bcl9* (Fig. 5Q) and *pygo2* (Fig. 5R), as well as the downstream Wnt/β-catenin targets *jun* (Fig. 5S) and *fosab* (Fig. 5T). Conversely, chromatin accessibility of these Wnt/β-catenin targets was dramatically

Development (2022) 149, dev200082. doi:10.1242/dev.200082

decreased in *prdm16*$^{-/-}$ (Fig. 5P-T). Areas of open chromatin aligned with areas of active gene expression identified by a previously published H3K27Ac ChIP-seq study of whole zebrafish embryos at 48 hpf (Bogdanovic et al., 2012). To determine whether *prdm3* and *prdm16* can directly bind to promoter regions of these canonical Wnt/β-catenin signaling component genes, cleavage under targets and release using nuclease paired with quantitative real-time PCR (CUT&RUN-RT-qPCR) was performed on whole zebrafish larvae at 48 hpf. Significant enrichment of Prdm3 and Prdm16 abundance was identified at putative binding sites for Prdm3 and Prdm16 near promoter regions of *ctnnb1* (Fig. 5U) and the downstream Wnt/β-catenin target gene *jun* (Fig. 5V). Only Prdm3 had significant enrichment at *fosab* (Fig. 5W), suggesting differences in target genes between Prdm3 and Prdm16. There was no enrichment of Prdm3 or Prdm16 at promoter regions of *bcl9* or *pygo2* (Fig. S7C,D). Although this result suggests that these factors may not be direct transcriptional targets of Prdm3 or Prdm16, this does not exclude a possible protein-protein interaction influencing Wnt/β-catenin enhanceosome activity indirectly. Taken together, these results suggest that Prdm3 and Prdm16 may not only influence transcription of Wnt/β-catenin signaling components by changing chromatin accessibility near promoter regions of these genes but may also affect expression of these Wnt/β-catenin genes by binding those targets directly. These results further emphasize opposing roles of Prdm3 and Prdm16 in facilitating a balance of canonical Wnt/β-catenin signaling during cranial NCC-derived chondrocyte differentiation in the craniofacial skeleton.

Pharmacological manipulation of canonical Wnt/β-catenin signaling in *prdm3*$^{-/-}$ and *prdm16*$^{-/-}$ zebrafish mutants partially restores chondrocyte stacking defects

Our genomic data suggest that Prdm3 and Prdm16 regulate Wnt activity in opposing ways to balance Wnt/β-catenin transcriptional activity during chondrocyte differentiation. We next sought to rescue cartilage phenotypes by pharmacological manipulation of Wnt signaling in both zebrafish mutants. To rescue the effects of elevated Wnt/β-catenin signaling in *prdm3* mutants, wild-type and *prdm3*$^{-/-}$ embryos were treated with either DMSO or 0.75 µM of the Wnt antagonist IWR-1 from 24 hpf to 48 hpf. IWR-1 blocks Wnt-induced β-catenin accumulation by stabilizing the Axin2 destruction complex (Chen et al., 2009). At 6 days post-fertilization (dpf), control and treated embryos were collected and stained with Alcian Blue and Alizarin Red to assess cartilage and bone (Fig. 6A-A‴). The chondrocytes in vehicle-treated *prdm3* mutants were highly disorganized (Fig. 6A′). IWR-1 treatment significantly restored chondrocyte organization within mutant cartilage structures (Fig. 6A‴), as quantified by measuring the angle between adjacent chondrocytes (Fig. 6B).

To mitigate the effects of decreased Wnt/β-catenin signaling in *prdm16*$^{-/-}$ larvae, wild-type and *prdm16*$^{-/-}$ embryos were treated with either DMSO or 0.05 µM of a Wnt/β-catenin agonist, GSK-3 inhibitor XV, from 24 hpf to 48 hpf. GSK Inhibitor XV blocks Gsk3-dependent phosphorylation of β-catenin, allowing for β-catenin stabilization. Whereas chondrocytes of *prdm16*$^{-/-}$ vehicle-treated larvae exhibited stacking defects (Fig. 6C,C′), Wnt/β-catenin activation completely rescued chondrocyte defects (Fig. 6C‴,D). GSK inhibition (canonical Wnt pathway activation) also completely rescued overall cartilage phenotypes in *prdm16*$^{-/-}$ mutants, including restoration of posterior ceratobranchial cartilages (Fig. S8A). Together, these results show that chondrocyte defects in *prdm3* and *prdm16* mutants can be restored by rebalancing Wnt/β-catenin signaling pharmacologically in each mutant.

Combined genetic loss of both *prdm3* and *prdm16* rescues chondrocyte stacking defects

Although our genomic data suggest that Prdm3 and Prdm16 regulate Wnt/β-catenin activity in opposing directions, we found that single loss of *prdm3* or *prdm16* causes similar cartilage phenotypes: defects in chondrocyte orientation, polarity, intercalation and growth. To determine whether genetic loss of both *prdm3* and *prdm16* would rescue or exacerbate the craniofacial cartilage phenotypes observed in the single mutants, double-homozygous *prdm3*$^{-/-}$;*prdm16*$^{-/-}$ mutants (and all other allelic combinations) were generated from *prdm3*$^{+/-}$;*prdm16*$^{+/-}$ heterozygous intercrosses (Fig. 6E-H). Surprisingly, loss of both *prdm3*$^{-/-}$ and *prdm16*$^{-/-}$ rescued the craniofacial phenotypes observed in single-mutant embryos with normal posterior arch cartilage structures, and partially restored the hypoplasia observed in other cartilage elements (Meckel's cartilages, trabeculae, ethmoid plate) (Fig. 6H,H′). *prdm3*$^{-/-}$;*prdm16*$^{-/-}$ double mutants also had a near-complete rescue of chondrocyte stacking and intercalation defects (Fig. 6H″,I). Combinatorial mutants in the allelic series did not rescue overall cartilage phenotypes or cellular stacking defects, suggesting that the rescue is dependent on complete loss of both paralogs (Fig. 6I, Fig. S8B,C). Although the near-complete rescue of cartilage defects was surprising in the double mutants, we did not fully assess the larval viability of the *prdm3*$^{-/-}$;*prdm16*$^{-/-}$ double mutants throughout later stages of larval development, juvenile growth and adulthood. Because Prdm3 and Prdm16 also function in other tissues, this rebalancing of gene expression would be required to also occur in these tissues in order for viability to be restored. Based on the latest stage of larval growth we did assess for cartilage phenotypes (6-8 dpf), *prdm3*$^{-/-}$;*prdm16*$^{-/-}$ double mutants phenotypically look healthy and indistinguishable from wild-type larvae, suggesting a possible rescue of viability. Future experiments will test this idea further. Together, these results emphasize the independent functional roles of Prdm3 and Prdm16 to balance GRNs and signaling modules, in particular canonical Wnt/β-catenin signaling, during craniofacial cartilage development.

DISCUSSION

In this study, we have identified functional roles for Prdm3 and Prdm16 in controlling proper chondrocyte differentiation by balancing canonical Wnt/β-catenin activity, both transcriptionally and epigenetically (Fig. 7). These two proteins have long been thought to act redundantly of each other, given their high amino acid sequence homology and similar developmental expression patterns. Contrary to this paradigm, our data highlight that each paralog has its own divergent and independent role in facilitating proper chondrocyte differentiation. Interestingly, Prdm3 and Prdm16 result from a vertebrate-specific duplication that occurred in the Gnathostomata ancestor (Vervoort et al., 2016). As such, independent functions of Prdm3 and Prdm16, at least in the case of chondrocyte maturation and bone differentiation in craniofacial development, may have coincided with their duplication event, which in turn correlates with the evolution of jawed vertebrates. In support of this idea, we hypothesize that, under normal developmental conditions during cranial NCC chondrocyte differentiation, Prdm3 functions as a traditional transcriptional repressor whereas Prdm16 acts as a non-traditional activator of gene expression to balance Wnt/β-catenin activity. Both mutants, despite their opposing transcriptomic profiles and chromatin landscape, have impaired chondrocyte orientation, polarity, intercalation and growth. Intriguingly, combined loss of both *prdm3* and *prdm16* dramatically rescues, rather than exacerbates, chondrocyte phenotypes. Furthermore, these results support a Prdm3- and

Development (2022) 149, dev200082. doi:10.1242/dev.200082

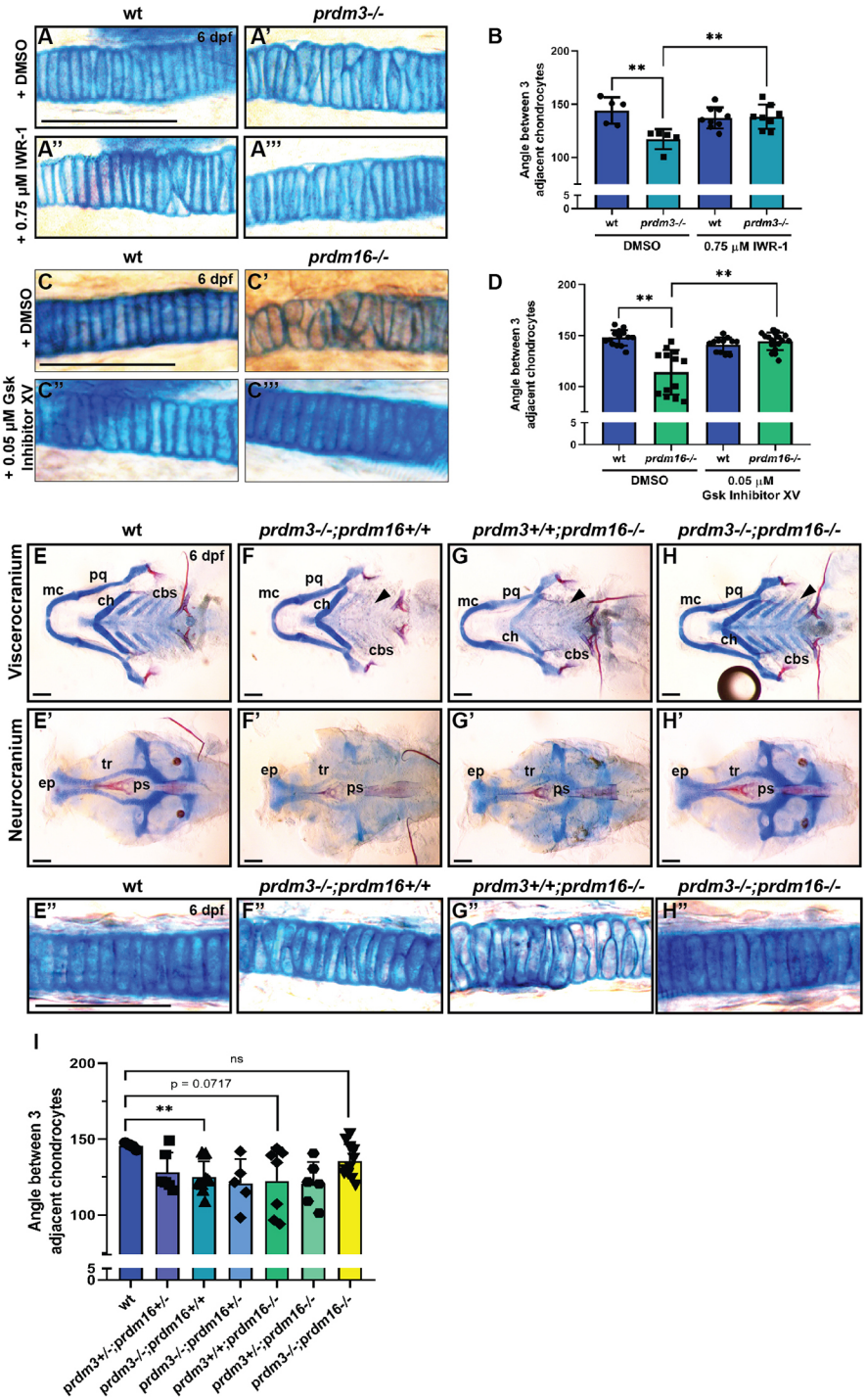

Fig. 6. Chondrocyte stacking defects with loss of *prdm3* and *prdm16* can be rescued by pharmacological manipulation of Wnt/β-catenin activity or genetically in *prdm3*$^{-/-}$;*prdm16*$^{-/-}$ double mutants. (A-B) Wild-type (wt) or *prdm3*$^{-/-}$ zebrafish embryos were treated with suboptimal doses of 0.75 µM IWR-1 or DMSO (vehicle control) from 24 to 48 hpf. Inhibitor- and vehicle-treated larvae were collected at 6 dpf and stained with Alcian Blue or Alizarin Red. (A-A‴) High magnification of chondrocytes within cartilage structures. (B) Quantification of chondrocyte organization (angle between adjacent cells) (*n*=at least 5 per genotype per treatment group); mean±s.d. Scale bars: 100 µm. (C-D) Wild-type (wt) or *prdm16*$^{-/-}$ embryos were treated with suboptimal doses of 0.05 µM Gsk inhibitor XV (Wnt activator) or DMSO (vehicle control) from 24 to 48 hpf. Larvae were collected at 6 dpf and stained with Alcian Blue and Alizarin Red. (C-C‴) High magnification of chondrocytes within cartilage elements. (D) Quantification of chondrocyte organization (*n*=at least 10 per genotype per treatment group); mean±s.d. Scale bar: 100 µm. (E-H″) *prdm3*$^{+/-}$;*prdm16*$^{+/-}$ heterozygous fish were generated and intercrossed. Larvae were collected at 6 dpf and stained with Alcian Blue and Alizarin Red. (E-H′) Dissected and mounted viscerocranium (E-H) and neurocranium (E′-H′) from wild type (E,E′), *prdm3*$^{-/-}$ (F,F′), *prdm16*$^{-/-}$ (G,G′) and *prdm3*$^{-/-}$;*prdm16*$^{-/-}$ double mutants (H,H′). (E″-H″) High magnification of chondrocytes in cartilage elements of wild type (E″), *prdm3*$^{-/-}$ (F″), *prdm16*$^{-/-}$ (G″) and *prdm3*$^{-/-}$;*prdm16*$^{-/-}$ double mutants (H″). cbs, ceratobranchials; ch, ceratohyal; ep, ethmoid plate; mc, Meckel's cartilage; pq, palatoquadrate; ps, parasphenoid; tr, trabeculae. (I) Quantification of the angle between adjacent chondrocytes across wild type, *prdm3*$^{-/-}$, *prdm16*$^{-/-}$ and *prdm3*$^{-/-}$;*prdm16*$^{-/-}$ double mutants, as well as all other combinatorial mutants indicated; mean±s.d. Scale bars: 100 µm. **$P \leq 0.005$; ns, not significant (unpaired, two-tailed Student's *t*-test).

Prdm16-dependent Wnt/β-catenin 'Goldilocks effect' during craniofacial chondrogenesis: there must be a precise level of Wnt/β-catenin activity during chondrocyte differentiation as too much or too little activity can have consequential effects on the proper maturation and differentiation of these cells.

Despite sharing similar craniofacial cartilage phenotypes, loss of *prdm3* or *prdm16* surprisingly causes drastically different changes to the transcriptome and chromatin accessibility. It will be interesting to investigate further whether these differences are due to an evolutionarily derived sub-functionalization or specialization of these proteins. It is also possible that Prdm factors have developed a sequence-level difference in specificity for their intrinsic methyltransferase activity. In addition to their methyltransferase abilities, both Prdm3 and Prdm16 commonly associate with other protein complexes to facilitate transcriptional regulation. Interestingly, there is very little overlap between known binding partners across both proteins, except for a few (Smad3, CtBP) (Palmer et al., 2001; Kajimura et al., 2009, 2008; Warner et al., 2007; Kurokawa et al., 1998). As such, the context of the protein complexes with which each Prdm is associated likely dictates how each Prdm influences gene expression and/or chromatin remodeling. Given the transcriptomic and chromatin accessibility changes we observe in each mutant, we predict that, perhaps at this developmental time point, Prdm3 is interacting in repressive complexes whereas Prdm16 is

Development (2022) 149, dev200082. doi:10.1242/dev.200082

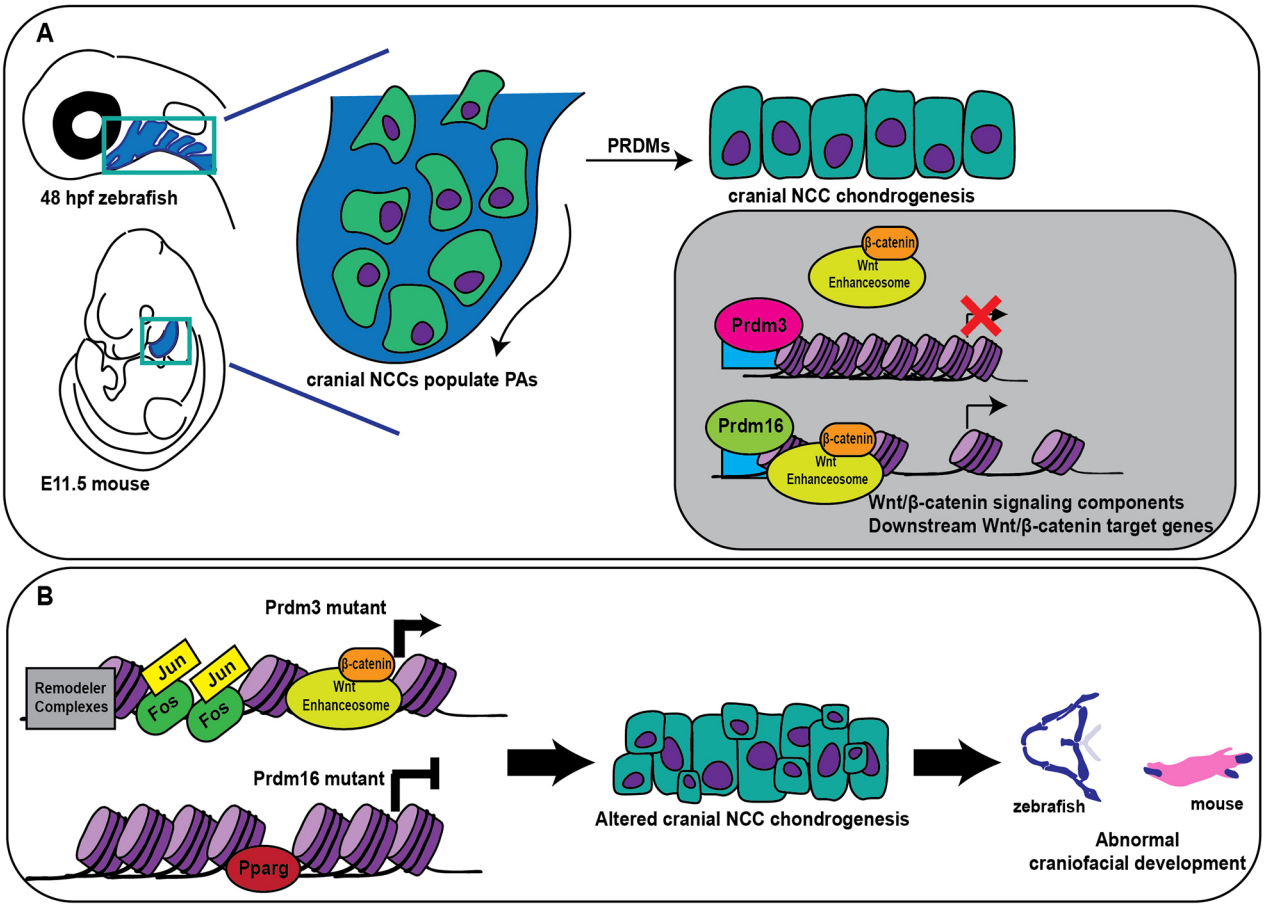

Fig. 7. Prdm3 and Prdm16 function upstream of Wnt/β-catenin to balance transcriptional activity during craniofacial chondrogenesis. (A) In vertebrates, Prdm3 and Prdm16 facilitate cranial NCC chondrocyte differentiation and maturation by balancing temporal and spatial Wnt/β-catenin transcriptional activity; Prdm3 acts a repressor of gene expression and Prdm16 acts as an activator of similar gene targets, particularly Wnt/β-catenin signaling components and downstream Wnt/β-catenin target genes. (B) Loss of Prdm3 leads to enhanced gene expression and increased occupancy of chromatin remodelers and Jun/Fos whereas loss of Prdm16 causes a dramatic decrease in gene expression and increased occupancy of Pparg, among others. In both cases, Wnt/β-catenin signaling is abrogated leading to altered cranial neural crest chondrocyte differentiation and maturation, which ultimately leads to abnormal development of craniofacial structures. PAs, pharyngeal arches.

associating more strongly with co-activating complexes. Teasing apart these diverging functional characteristics and the potential for transient changes to these roles over developmental time will facilitate a better understanding of the specific molecular mechanisms of these Prdm factors in craniofacial cartilage development.

Mechanisms of transcriptional adaptation have been used to explain genetic compensation between genetic alleles derived from CRISPR gene editing. We have observed some level of genetic compensation in both *prdm3* and *prdm16* mutants, whereby *prdm16* is modestly elevated in *prdm3* mutants (Shull et al., 2020). However, *prdm3* is decreased in *prdm16* mutants. Interestingly, expression of a third Prdm family member, *prdm1a*, is increased in both *prdm3* and *prdm16* single mutants and combined loss of all three alleles causes drastically more severe craniofacial phenotypes (Shull et al., 2020). As such, it is possible that genetic interactions or feedback regulatory loops between these alleles could also influence the phenotypes we observe in these single mutants.

We have identified a GRN centered on balancing temporal and spatial canonical Wnt/β-catenin signaling during cartilage development that is facilitated by Prdm3 and Prdm16. We hypothesize that there are several mechanisms, both direct and indirect, that may be driving this temporal regulation. Among the differentially expressed Wnt/β-catenin signaling components, the members of the Wnt enhanceosome transcriptional complex, in particular the intermediary protein that facilitates β-catenin nuclear localization and assembly of the Wnt enhanceosome complex, *bcl9/bcl9l*, and its binding partner, *pygo1/2*, were significantly altered in both *prdm3* and *prdm16* zebrafish mutants. Previous work has shown that *bcl9* zebrafish mutants have cranial NCC defects, including craniofacial cartilage phenotypes (Cantu et al., 2018). It would be interesting to determine whether Prdm3 and Prdm16 participate in the Wnt enhanceosome transcriptional complex through protein interactions with members of the complex, including *bcl9/bcl9l*, *pygo1/2*, or others to influence Wnt/β-catenin transcriptional activity. It could be possible that Prdm3 and Prdm16 are downstream Wnt/β-catenin transcriptional targets that would form a regulatory circuit, which could facilitate the timely gradient of Wnt/β-catenin necessary during chondrocyte differentiation and maturation during craniofacial development.

Although we have focused only on canonical Wnt/β-catenin signaling, it is possible that non-canonical Wnt/planar cell polarity (PCP) signaling is also active. Recent studies have suggested that crosstalk between the two pathways coordinates developmental processes (Navajas Acedo et al., 2019). In alignment with these studies, we did observe changes in several Wnt/PCP genes (*vangl2*, *scrib*, *fat*) as well as the transcription factors Jun/Fos. Although *jun*

Development (2022) 149, dev200082. doi:10.1242/dev.200082

and *fos* are direct canonical Wnt/β-catenin target genes, they are also activated in response to non-canonical Wnt/PCP through JNK signaling. Because both *prdm3* and *prdm16* mutants share cartilage phenotypes similar to those observed in PCP zebrafish mutants, we speculate that Prdm3 and Prdm16 could also control crosstalk between both canonical and non-Wnt/β-catenin signaling activity during chondrocyte differentiation.

Finally, we define conserved functions of Prdm3 and Prdm16 across vertebrates. We show that loss of *Prdm3* and *Prdm16* in the murine neural crest lineage disrupts Meckel's cartilage chondrocyte organization and maturation owing to dysregulated Wnt/β-catenin signaling during early chondrogenesis in the mandibular facial processes. We hypothesize that this abnormal chondrocyte maturation could impact the development of the mandible, which could explain the anterior mandibular hypoplasia seen in these animals. It will be interesting to understand further how Prdm3 and Prdm16 regulate this potential coupling mechanism between chondrocyte maturation and subsequent bone formation in the developing mandible.

In summary, we have defined the roles for the chromatin modifiers Prdm3 and Prdm16 in cranial neural crest development and formation of the craniofacial skeleton. We show that these two seemingly functional redundant paralogs can act antagonistically independent of each other upstream of canonical Wnt/β-catenin signaling during chondrocyte differentiation to ensure proper spatial and temporal development of the vertebrate craniofacial skeleton.

MATERIALS AND METHODS

Zebrafish

Zebrafish were maintained as previously described (Westerfield, 2007) in accordance with standard zebrafish husbandry conditions. Embryos were raised in defined Embryo Medium at 28.5°C and staged developmentally following published standards as described (Kimmel et al., 1995). The wild-type strain used was the AB line (ZIRC). The transgenic lines used were *Tg(−4.9sox10:EGFP)* (Dutton et al., 2008), *Tg(fli1:EGFP)* (Lawson and Weinstein, 2002) and *Tg(7xTCF-Xla.Sia:NLS-mCherry)*^{ia5Tg} (Moro et al., 2012). These transgenic lines were crossed to the various mutant backgrounds. Zebrafish mutant lines for *prdm3* and *prdm16* were generated by CRISPR-based mutagenesis as previously described (Shull et al., 2020). The *prdm3* and *prdm16* mutant alleles used in this study (*prdm3*^{CO1005} and *prdm16*^{CO1006}) are predicted frameshift mutations that interrupt the coding sequence upstream of the PR/SET domain responsible for functional histone methyltransferase activity (Shull et al., 2020). For double mutants, *prdm3*$^{+/−}$ fish were bred to *prdm16*$^{+/−}$ fish to generate *prdm3*$^{+/−}$*;prdm16*$^{+/−}$ double-heterozygous animals, which were intercrossed to generate *prdm3*$^{−/−}$*;prdm16*$^{−/−}$ double mutants as well as all the other resulting various allelic combinatorial animals. All experiments were completed on zebrafish embryos or larvae before sex was determined in these animals (20 dpf). The Institutional Animal Care and Use Committee of the University of Colorado Anschutz Medical Campus approved all animal experiments performed in this study and the procedures conform to NIH regulatory standards of care.

Mice

Mecom^{tm1mik} (referred to as *Prdm3*$^{fl/fl}$) (Goyama et al., 2008), *B6(SJL)-Prdm16*$^{tm1.1Snok}$*/J* (referred to as *Prdm16*$^{fl/fl}$) (The Jackson Laboratory) and *H2afv*$^{Tg(Wnt\text{-}Cre)11Rth}$ (referred to as *Wnt1-Cre*$^{+/Tg}$) (Danielian et al., 1998) were all maintained on the C57/Bl6 background and housed at a sub-thermoneutral temperature (21-23°C) under a 12 h light/dark cycle with water and food (PicoLab Rodent Diet 20) provided *ad libitum*. For timed matings, *Prdm3*$^{fl/fl}$ or *Prdm16*$^{fl/fl}$ females were bred to *Prdm3*$^{fl/+}$*;Wnt1-Cre*$^{+/Tg}$ or *Prdm16*$^{fl/+}$*;Wnt1-Cre*$^{+/Tg}$ males, respectively. The morning a vaginal plug was detected was considered E0.5. Embryos of matching somite numbers were used for experiments. Mice were euthanized by carbon dioxide inhalation followed by cervical dislocation as a secondary method of euthanasia. Male and female embryos were analyzed in this study and there were no sex-dependent differences in phenotypes between the two groups. Developmental stages of embryos used are indicated in the results. All embryos were stage-matched by somite counting. Mice were bred and maintained in accordance with the recommendations in the Guide for the Care and Use of Laboratory Animals of the National Institutes of Health. The protocol was approved by the University of Colorado Anschutz Medical Campus's Institutional Animal Care and Use Committee.

Genotyping

Fin clips, single whole embryos or single embryo larva tails were lysed in lysis buffer [10 mM Tris-HCl (pH 8.0), 50 mM KCl, 0.3% Tween-20, 0.3% NP-40, 1 mM EDTA] for 10 min at 95°C, incubated with 50 ug of Proteinase K at 55°C for 2 h, followed by inactivation of Proteinase K at 95°C for 10 min. Genotyping for *prdm3* and *prdm16* mutant alleles was performed as previously described (Shull et al., 2020). See Table S6 for genotyping primers.

For mice, tail clips from weanlings and tail clips or yolk sacs from embryos were lysed in DNA lysis buffer [10 mM Tris-HCl (pH 8.0), 100 mM NaCl, 10 mM EDTA (pH 8.0), 0.5% SDS] and 100 µg of Proteinase K overnight at 55°C. Genomic DNA was isolated following phenol/chloroform extraction. DNA pellets were air-dried and re-suspended in nuclease-free water. Genotyping for *Prdm3*, *Prdm16* and *Wnt1-Cre* alleles was performed as previously described (Shull et al., 2020). See Table S6 for genotyping primers.

Inhibitor treatments

For inhibitor treatment experiments, embryos were dechorionated at 24 hpf. The clutches were divided evenly into two groups: vehicle control or inhibitor treatment groups. *Prdm3* heterozygous intercrossed embryos were treated with either the Wnt inhibitor IWR-1 (Sigma-Aldrich), at a final concentration of 0.75 µM, or DMSO, in E2 embryo water. *Prdm16* heterozygous intercrossed embryos were treated with either the Wnt activator Gsk inhibitor XV (CalbioChem), at a final concentration of 0.05 µM, or DMSO for vehicle control, in E2 embryo water. Inhibitor- or vehicle-containing E2 embryo water was removed after a 24-h window (at 48 hpf developmental time) and replaced with fresh E2 embryo water. At 6 dpf, larvae were collected and fixed in 2% paraformaldehyde (PFA) and subjected to Alcian Blue/Alizarin Red staining for cartilage and bone assessment.

Skeletal staining

For zebrafish, Alcian Blue (cartilage) and Alizarin Red (bone) staining was performed at room temperature as previously described (Walker and Kimmel, 2007). Briefly, 6 dpf larvae were collected and fixed for 1 h in 2% PFA. Following a 10-min rinse in 100 mM Tris (pH 7.5) and 10 mM $MgCl_2$, larvae were incubated in Alcian Blue solution [0.04% Alcian Blue, 80% ethanol, 100 mM Tris (pH 7.5), 10 mM $MgCl_2$] overnight at room temperature. Larvae were then rehydrated and de-stained through a gradient of ethanol solutions [80%, 50%, 25% ethanol containing 100 mM Tris (pH 7.5) and 10 mM $MgCl_2$], then bleached for 10 min in 3% H_2O_2 with 0.55% KOH at room temperature, washed twice in 25% glycerol with 0.1% KOH, then stained in Alizarin Red [0.01% Alizarin Red dissolved in 25% glycerol and 100 mM Tris (pH 7.5)] for 30-45 min at room temperature. Samples were de-stained in 50% glycerol with 0.1% KOH. Whole-mount and dissected and flat-mounted specimens were mounted in 50% glycerol and imaged with LAS v4.4 software on a Leica M165 FC stereomicroscope. High-magnification images of chondrocytes were imaged with LAS v4.4 software on an Olympus BX51 WI compound microscope.

For mice, Alcian Blue and Alizarin Red staining was performed as previously described for E18.5 embryos (Wallin et al., 1994; Shull et al., 2020). Briefly, mouse embryos were harvested at E18.5 in 1×PBS. Skin and internal organs were removed, and specimens were fixed overnight in 95% ethanol at room temperature followed by an incubation in 100% acetone for 2 days at room temperature. Embryos were then stained in Alcian Blue/Alizarin Red staining solution (0.015% Alcian Blue, 0.05% Alizarin Red, 5% glacial acetic acid and 70% ethanol) for 3 days at 37°C. Stained embryos

Development (2022) 149, dev200082. doi:10.1242/dev.200082

were rinsed in water before undergoing an initial clearing in 1% KOH overnight at room temperature, followed by a gradient series of decreasing KOH concentrations and increasing glycerol concentrations. Skeletal preparations were stored and imaged in 80% glycerol on a Leica M165 FC stereomicroscope with LASX v4.4 software.

Histology

Mouse embryos were collected at E14.5 in 1×PBS. The mandible was dissected and removed from the heads of the animals and fixed in 4% PFA, cryoprotected in 30% sucrose solution, embedded in OCT embedding medium, sectioned to a thickness of 8 µm and mounted onto glass slides with a Leica CM1520 cryostat. For staining, sections were brought to room temperature and rehydrated in 1×PBS before staining with Weigert's iron Hematoxylin, 0.05% Fast Green and 0.1% Safranin O and mounted with Permount (Electron Microscopy Sciences). Stained sections were imaged on an Olympus BX51 WI compound microscope with LASX v4.4 software.

FACS of neural crest cells

At 48 hpf, *sox10:EGFP*-positive embryos were stage-matched and selected under a fluorescence dissecting microscope. *prdm3*$^{-/-}$*;Tg(sox10:EGFP)* and *prdm16*$^{-/-}$*;Tg(sox10:EGFP)* single-mutant embryos were identified based on their phenotype (small domed heads and reduced eye pigmentation) at 48 hpf and extensively validated and confirmed by genotyping so that mutant embryos could be identified for FACS and subsequent sequencing experiments (Fig. S9). To prepare single-cell suspensions for FACS, 30-40 embryos of each genotype were dechorionated and rinsed in 1× DPBS (Ca^{2+} and Mg^{2+} free). Embryos were then dissociated in Accumax (Innovative Cell Technologies, AM-105) containing DNaseI (Roche Diagnostics). The samples were incubated at 31°C and agitated by pipetting every 10-15 min for 1 h to promote cell dissociation. Following the digest, a wash solution (1× D-PBS and DNaseI) was added to stop the reaction. Cells were filtered through a 70 µm nylon mesh strainer, centrifuged at 2000 rpm (376 ***g***) for 5 min at 4°C and resuspended in FACS basic sorting buffer [1 mM EDTA, 25 mM HEPES (pH 7.0), 1% fetal bovine serum in 1× D-PBS]. Cell suspensions were stained with DAPI (1:1000) and kept on ice. GFP-positive cells were sorted on a MoFlo XDP100 cell sorter (Beckman-Coulter) and collected in 1× DPBS. Following FACS, GFP-positive cells were then processed for RNA-seq or ATAC-seq.

RNA-seq

Following FACS, GFP-positive NCCs were centrifuged briefly at 2000 rpm (376 ***g***) for 5 min and resuspended in TRIzol LS lysis reagent (Invitrogen/Life Technologies). Total RNA was extracted from sorted cells using chloroform extraction and the Direct-zol RNA miniprep kit (Zymo Research) according to the manufacturer's instructions. Purified RNA quality and quantity was assessed on a High Sensitivity RNA Screen Tape (Agilent Technologies) and Infinite M200pro plate reader (Tecan). cDNA libraries were generated using the Clontech Pico Library Prep Kit. Following library generation, sequencing was performed on an Illumina NovaSEQ 6000 system to a depth of ∼50 million reads. Library construction and sequencing was performed at the University of Colorado Anschutz Medical Campus Genomics and Microarray Core Facility.

RNA isolation and RT-qPCR

For zebrafish, whole heads were dissected and removed from wild-type, *prdm3*$^{-/-}$ and *prdm16*$^{-/-}$ embryos at 48 hpf. Five to seven embryos of the same genotype were pooled and lysed in TRIzol LS lysis reagent (Invitrogen/Life Technologies). Total RNA was isolated following a chloroform extraction. For mice, mandibular processes (MdPs) were dissected on ice from three independent replicates of E11.5 *Prdm3*$^{fl/fl}$*;Wnt1-Cre*$^{+/Tg}$, *Prdm16*$^{fl/fl}$*;Wnt1-Cre*$^{+/Tg}$ and control (*Prdm3*$^{fl/fl}$ or *Prdm16*$^{fl/fl}$) embryos. The overlying ectoderm was removed by digestion in 0.25% trypsin for 10-15 min on ice. MdPs were rinsed in 10% FBS for 1 min before a quick rinse in 1×PBS. MdPs were lysed in TRIzol LS (Invitrogen/Life Technologies) and total RNA was isolated from these samples using the Direct-zol RNA miniprep kit (Zymo Research) according to the manufacturer's instructions.

For RT-qPCR, total RNA was isolated as described above for zebrafish and mouse MdPs and (0.5-1.0 µg) was reverse transcribed to cDNA with SuperScript III First-Strand Synthesis cDNA kit (Invitrogen/Life Technologies) for real-time semiquantitative PCR (RT-qPCR) with primers (Table S5) and SYBR Green Master Mix (Bio-Rad). Transcript levels were normalized to the reference gene, *gapdh* (zebrafish) or *Actb* (mouse). Transcript abundance and relative gene expression were quantified using the $2^{-\Delta\Delta Ct}$ method relative to control.

ATAC-seq

ATAC-seq was performed as previously described (Buenrostro et al., 2015; Liu et al., 2020). Briefly, following tissue dissociation FACS (as described above), 25,000 GFP-positive cells per genotype were pelleted at 500 ***g*** for 5 min at 4°C. The cell pellets were gently resuspended in cold lysis buffer (10 mM Tris-HCl, pH 7.5, 10 mM NaCl, 3 mM $MgCl_2$, 0.1% v/v NP-40). Lysed cells were immediately centrifuged at 500 ***g*** for 20 min at 4°C. Cell nuclei pellets were resuspended in tagmentation mix with Nextera Tagmentation Buffer (Illumina) and Nextera Tagmentation DNA Enzyme (Illumina). Tagmentation reactions were adjusted to accommodate 25,000 cells and incubated at 37°C for 30 min, mixing at 10 min intervals. Tagmented DNA was purified using the Zymogen DNA Clean and Concentrator kit (Zymo Research). Libraries were amplified and indexed using NEBNext High Fidelity 2× PCR master mix (New England Biolabs). Following 11 cycles of amplification, libraries were purified with AmpureXP beads (Beckman Coulter), quantified with Qubit and subjected to sequencing on the Illumina NovaSEQ 6000 system at a depth of ∼50 million reads at the University of Colorado Anschutz Medical Campus Genomics and Microarray Core Facility. ATAC-seq experiments were performed in duplicate for two biological replicates per genotype.

CUT&RUN paired with RT-qPCR

CUT&RUN was performed on wild-type whole embryos as described (Skene and Henikoff, 2017). Briefly, ∼200 48 hpf wild-type zebrafish embryos were pooled and dissociated to a single-cell suspension using Accumax (Innovative Cell Technologies) and DNaseI (Roche Diagnostics) for 1 h with gentle pipetting to agitate the tissue every 10 min. Following dissociation, a wash solution containing 1×PBS and DNaseI was added to stop the reaction. Cells were passed through a 40 µm filter and counted then 500,000 cells were incubated on activated Concanavalin A conjugated paramagnetic beads (Epicypher) for 10 min at room temperature. Cell-bound beads were resuspended in antibody buffer [20 mM HEPES, pH 7.5; 150 mM NaCl; 0.5 mM Spermidine (Invitrogen); 1× Complete-Mini Protease Inhibitor tablet (Roche Diagnostics); 0.01% Digitonin (Sigma-Aldrich); 2 mM EDTA] and incubated in the corresponding antibodies (validated to work in zebrafish; see Fig. S7A,B). Although validated, we cannot rule out the possibility that these antibodies may to a lesser extent recognize other proteins of similar size to the wild-type band. Antibodies [IgG (Jackson ImmunoResearch, 111-005-003, RRID: AB_2337913), Prdm3/Evi1 (Abcam, ab28457, RRID: AB_732271), Prdm16 (antibody gifted from Patrick Seale, University of Pennsylvania, USA; R&D Systems, AF6295, RRID: AB_10717965) and H3K27ac (Cell Signaling Technology, 4353S, RRID: AB10545273)] were added to samples and incubated overnight with rotation at 4°C. The following day, cells were washed in Digitonin Buffer wash solution [20 mM HEPES, pH 7.5; 150 mM NaCl; 0.5 mM Spermidine (Sigma-Aldrich); 1× Complete-Mini Protease Inhibitor tablet (Roche Diagnostics); 0.01% Digitonin (Sigma-Aldrich)] twice and then incubated with pAG-MNase (EpiCypher) for 10 min at room temperature. Following another two washes in Digitonin Buffer, 1 µl of 100 mM $CaCl_2$ was added to each sample and incubated at 4°C for 2 h. This digestion reaction was stopped with the addition of Stop Buffer (340 mM NaCl, 20 mM EDTA, 4 mM EGTA, 50 µg/ml RNaseA and 50 µg/ml glycogen) for 10 min at 37°C. DNA fragments were purified using a DNA Clean and Concentrator Kit (Zymo Research). For RT-qPCR, eluted CUT&RUN fragmented DNA was amplified using the NEBNext Ultra II

Development (2022) 149, dev200082. doi:10.1242/dev.200082

DNA Library Prep Kit (New England Biolabs) as per the manufacturer's instructions. RT-qPCR was performed with primers designed to flank putative Prdm3 and Prdm16 binding motifs at promoter regions of Wnt/β-catenin targets genes or negative control genes with no binding sites (*gapdh*) and SYBR Green Master Mix (Bio-Rad). The fold enrichment for the abundance of Prdm3, Prdm16 or H3K27ac of those amplified regions was calculated and normalized relative to the IgG control and averaged across three different experiments.

Whole-mount immunofluorescence

Zebrafish larvae were collected at the indicated time points and fixed in 4% PFA overnight at 4°C. Following fixation, embryos were washed in 1× PBS (pH 7.3) with 1% Triton X-100 three times for 10 min at room temperature. For antigen retrieval, embryos were incubated in 1 µg/ml Proteinase K diluted in 1× PBS with 1% Triton X-100 for 20 min at room temperature. Following proteinase K treatment, embryos were incubated in 4% PFA for 15 min at room temperature, then washed three more times in 1× PBS with 1% Triton X-100 for 10 min at room temperature. Embryos were blocked at room temperature for 1 h in blocking solution containing 10% normal goat serum and 1% bovine serum albumin in 1× PBS. Samples were incubated in primary antibodies diluted (1:100) in blocking solution [anti-acetylated α-tubulin (Sigma-Aldrich, T6793, RRID: AB_477585), anti-phosphorylated Y489 β-catenin (Developmental Studies Hybridoma Bank, PY489-B-catenin, RRID: AB_732271), Rhodamine phalloidin (Thermo Fisher, R415, RRID: AB_2572408), Wheat Germ Agglutinin (Life Technologies/Invitrogen, W32466)], overnight at 4°C. Following primary antibody incubation, samples were thoroughly washed in PBS with 1% Triton X-100 before incubating with corresponding secondary antibodies overnight at 4°C, then were washed again thoroughly in 1× PBS with 1% Triton X-100 before incubation with DAPI diluted in 1× PBS for 1 h at room temperature. Samples were quickly washed in PBS with 1% Triton X-100 before being mounted in Vectashield mounting media (Invitrogen) on glass slides. Embryos were imaged on a Leica TCS SP8 confocal microscope. Images were processed using LASX software and ImageJ.

Whole-mount immunohistochemistry

Whole-mount immunohistochemistry on mouse embryos was performed as previously described (Joyner and Wall, 2008). Briefly, E10.5 or E11.5 wild-type embryos were dissected in 1× PBS and fixed in methanol/DMSO (4:1) at 4°C overnight. Embryos were then transferred to methanol/DMSO/H_2O_2 (4:1:1) and incubated at room temperature for 8 h. Embryos were rehydrated at room temperature through a series of washes: 50% methanol for 30 min, 1×PBS for 30 min and PBSMT (2% nonfat instant skim milk, 0.5% Triton X-100 in 1×PBS) for 1 h. Specimens were then incubated in primary antibodies diluted 1:200 in PBSMT [Prdm3 (Abcam, ab28457, RRID: AB_732271), Prdm16 (Patrick Seale, University of Pennsylvania; R&D Systems, AF6295, RRID: AB_10717965)] overnight at 4°C with rocking. Embryos were then washed. Samples were incubated in secondary antibodies diluted 1:500 in PBSMT [HRP-conjugated goat anti-rabbit IgG (Santa Cruz Biotechnology, sc-2004, RRID: AB_631746)] overnight at 4°C with rocking. Embryos were washed again in PBSMT twice, 1 h each, at 4°C followed by three times, 1 h each, at room temperature and then rinsed and washed in PBTX (0.2% w/v bovine serum albumin, 0.5% v/v Triton X-100, 1×PBS) for 20 min. Samples were then incubated in DAB-$NiCl_2$ (3,3′-diaminobenzidine tetrahydrochloride, $NiCl_2$ in 1×PBS) for 30 min at room temperature. Hydrogen peroxide was added to a final concentration of 0.03% and the samples were rocked until the color developed (5 min), then post-fixed in 4% PFA. Samples were then rinsed through a methanol gradient and then incubated in BABB (benzyl benzoate/benzyl alcohol 2:1) for 10 min. Stained embryos were imaged on a Leica M165 FC stereomicroscope with LASX v4.4 software.

Western blotting

Zebrafish embryos (30-40) of each genotype were pooled at 48 hpf and incubated on ice for 5 min. Calcium-free Ginzberg Fish Ringer's solution (55 mM NaCl, 1.8 mM KCl, 1.25 mM $NaHCO_3$) was added to the embryos for deyolking. After pelleting samples for 1.5 min at 5000 rpm (2348 ***g***), samples were washed in deyolking wash buffer [110 mM NaCl, 3.5 mM KCl, 2.7 mM $CaCl_2$, 10 mM Tris (pH 8.5)]. Samples were pelleted again for 1.5 min at 5000 rpm (2348 ***g***). All liquid was removed and the pellet was resuspended in SDS lysis buffer [0.1% glycerol, 0.01% SDS, 0.1 M Tris (pH 6.8)] for 10 min on ice. Embryos were homogenized in lysis buffer and again briefly centrifuged at 2348 ***g*** for 5 min. Total protein concentrations were determined using the Bio-Rad Dc Protein Assay (Bio-Rad). Proteins (20 µg) were separated by SDS-PAGE (12%) and transferred to polyvinylidene difluoride membranes. Membranes were blotted using antibodies for Prdm3 (Abcam, ab28457, RRID: 732271), Prdm16 (antibody gifted from Patrick Seale Lab, University of Pennsylvania, USA; R&D Systems, AF6295, RRID: AB_10717965) and total H3 (Cell Signaling Technology, 9715S, RRID: AB_331563) diluted at 1:1000 and corresponding secondary antibodies. Chemiluminescence detection was performed with Immobilon Forte Western HRP Substrate (Millipore) on a Bio-Rad Chemidoc multiplex imager.

Time-lapse imaging

Zebrafish embryos were imaged on a Leica DMi8 microscope equipped with an Andor Dragonfly 301 spinning disk confocal system. Approximately 100 µm *z*-stacks were captured at 0.35 µm intervals every 30 min for approximately 16 h. ImageJ was used for image processing.

Quantification and statistical analysis

RNA-seq bioinformatics analysis

Following trimming and read alignment, paired-end reads were mapped to the zebrafish genome (danRer11) assembly using TopHat (Trapnell et al., 2009, 2012). Differential expression between mutant and wild type was calculated using Cufflinks (Trapnell et al., 2012). Gene expression was expressed in fragments per kilobase of transcript per million mapped reads (FPKM). Complete RNA-seq datasets are available at the Gene Expression Omnibus repository (GSE175767). Normalized counts were converted to *z*-scores for plotting heatmaps using the pheatmaps R package (https://cran.r-project.org/web/packages/pheatmap/index.html). Gene lists were analyzed for functional annotation using GO enrichment analysis based on the PANTHER Classification System (Mi et al., 2019a,b; Ashburner et al., 2000; Harris et al., 2004).

ATAC-seq bioinformatics analysis

Adapters and barcodes were removed from paired end reads using Cutadapt (Martin, 2011), and trimmed paired-end sequencing reads were aligned to the zebrafish genome (danRer11) using Bowtie2 (v2.4.4) with default parameters (–end-to-end, –sensitive) (Langmead and Salzberg, 2012; Langmead et al., 2019). Peaks were called for each sample using the Genrich peak calling program (https://github.com/jsh58/Genrich), with the following parameters: -r, -p0.01, -a200, -j, -e MT. Intersection peaksets were generated for each genotype (e.g. Prdm3 mutant, Prdm3 wild type, Prdm16 mutant, Prdm16 wild type) by using bedtools (v.2.30.0) or bedops (v.2.4.37) to identify the sets of peaks observed in both replicates of each genotype. DiffBind (v.3.4.0) was used to assess differentially accessible regions between genotypes and their respective sibling controls using the default parameters [false discovery rate (FDR)≤0.05] (Ross-Innes et al., 2012). For volcano plots, −log(pvalue) was used for visualization of the data. Annotation of peaks corresponding to transcription start site (TSS)/promoter, intergenic, intronic and transcription end site (TES) locations was carried out using HOMER (v4.11) annotatePeaks.pl script (Heinz et al., 2010). DeepTools (v2.0) was used to generate bigWig coverage files for visualization (normalization=counts per million) (Ramirez et al., 2016). TOBIAS was performed following the standard pipeline and workflow (Bentsen et al., 2020). Complete ATAC-seq datasets are available in the GEO repository (GSE175767).

Image quantification

To quantify chondrocyte organization from Alcian-stained and dissected flat mounts, high-magnification images of cartilage elements were imported into ImageJ. An angle was drawn from the center of three adjacent chondrocytes moving along the cartilage element in the direction of growth of that structure. Angles were measured and averaged across at least five cartilage elements (namely the posterior ceratobranchial cartilages) per

individual. All possible combinations were measured within the field of view to eliminate any possible cell-selection bias.

To quantify chondrocyte cell orientation, individual chondrocytes in the developing palatoquadrate were divided into quadrants in ImageJ. The positioning of acetylated α-tubulin puncta was indicated as either 0°, 90°, 180° or 270° in the direction of growth of the palatoquadrate, i.e. anteriorly toward the jaw joint junction with the Meckel's cartilage. Positioning was tracked through *z*-stack images and the number of acetylated α-tubulin puncta in each quadrant was tabulated for each individual and normalized to the total number of cells analyzed for that individual. Total counts were collected for at least five individuals per genotype then averaged across genotypes and plotted as circular graphs. Nuclear β-catenin puncta (phosphorylated Y489 β-catenin) were quantified and tracked across ten chondrocytes in the palatoquadrate through *z*-stack images for one individual. The number of puncta was averaged for each individual and at least five individuals were analyzed per genotype.

For quantifying chondrocyte cell area in mouse Meckel's cartilage, the area of 200 cells across four or five sections anterior to posterior through the tissue were measured and averaged across three individuals per genotype. For cell numbers, cells were counted in a designated region of tissue area across four or five sections anteriorly to posteriorly throughout the tissue and averaged across three individuals per genotype.

Statistical analysis

Data shown are mean±s.d. from the number samples or experiments indicated in the figure legends. All assays were repeated at least three times with independent samples. *P*-values were determined with unpaired, two-tailed Student's *t*-tests.

Acknowledgements

We thank members of the Artinger laboratory for their thoughtful discussions on this project and Dr Richard Dorsky for the *Tg(7xTCF-Xla.Siam:NLS-mCherry)* line. We would also like to acknowledge undergraduates Oscar Yip and Joey Gerlach for their contributions to this work. We thank Kristen D'Elia and Drs Jeremy Dasen and David Schoppik at New York University for their feedback and insightful comments on this project. Special thanks to Dr David Clouthier for mouse craniofacial anatomy consultation. We thank the Denver zebrafish community, and the zebrafish and mouse facility staff for excellent animal care. The Functional Genomics and Biostatistics and Bioinformatics were funded by National Cancer Institute shared resource (P30CA046934 to the University of Colorado Cancer Center).

Competing interests

The authors declare no competing or financial interests.

Author contributions

Conceptualization: L.C.S., K.B.A.; Methodology: L.C.S., K.B.A.; Formal analysis: L.C.S., E.S.L., H.M.K., J.C.C., K.J.; Investigation: L.C.S., E.S.L.; Resources: S.G., M.K.; Writing - original draft: L.C.S., K.B.A.; Writing - review & editing: L.C.S., E.S.L., J.C.C., K.B.A.; Supervision: K.B.A.; Funding acquisition: L.C.S., K.B.A.

Funding

Funding was provided by the National Institute of Dental and Craniofacial Research (R01 DE024034 to K.B.A. and F32 DE029099 to L.C.S.) and the National Institute of Neurological Disorders and Stroke (P30 NS048154 to the UC Anschutz Medical Campus zebrafish core facility). Deposited in PMC for release after 12 months.

Data availability

The RNAseq and ATACseq datasets generated in this paper are available at Gene Expression Omnibus under accession number GSE175767.

Peer review history

The peer review history is available online at https://journals.biologists.com/dev/article-lookup/doi/10.1242/dev.200082.

References

Arai, S., Yoshimi, A., Shimabe, M., Ichikawa, M., Nakagawa, M., Imai, Y., Goyama, S. and Kurokawa, M. (2011). Evi-1 is a transcriptional target of mixed-lineage leukemia oncoproteins in hematopoietic stem cells. *Blood* **117**, 6304-6314. doi:10.1182/blood-2009-07-234310

Ashburner, M., Ball, C. A., Blake, J. A., Botstein, D., Butler, H., Cherry, J. M., Davis, A. P., Dolinski, K., Dwight, S. S., Eppig, J. T. et al. (2000). Gene ontology: tool for the unification of biology. The Gene Ontology Consortium. *Nat. Genet.* **25**, 25-29. doi:10.1038/75556

Baizabal, J.-M., Mistry, M., García, M. T., Gómez, N., Olukoya, O., Tran, D., Johnson, M. B., Walsh, C. A. and Harwell, C. C. (2018). The epigenetic state of PRDM16-regulated enhancers in radial glia controls cortical neuron position. *Neuron* **99**, 239-241. doi:10.1016/j.neuron.2018.06.031

Ben-Ze'ev, A. and Geiger, B. (1998). Differential molecular interactions of beta-catenin and plakoglobin in adhesion, signaling and cancer. *Curr. Opin. Cell Biol.* **10**, 629-639. doi:10.1016/S0955-0674(98)80039-2

Bentsen, M., Goymann, P., Schultheis, H., Klee, K., Petrova, A., Wiegandt, R., Fust, A., Preussner, J., Kuenne, C., Braun, T. et al. (2020). ATAC-seq footprinting unravels kinetics of transcription factor binding during zygotic genome activation. *Nat. Commun.* **11**, 4267. doi:10.1038/s41467-020-18035-1

Biosse Duplan, M., Komla-Ebri, D., Heuzé, Y., Estibals, V., Gaudas, E., Kaci, N., Benoist-Lasselin, C., Zerah, M., Kramer, I., Kneissel, M. et al. (2016). Meckel's and condylar cartilages anomalies in achondroplasia result in defective development and growth of the mandible. *Hum. Mol. Genet.* **25**, 2997-3010. doi:10.1093/hmg/ddw153

Bjork, B. C., Turbe-Doan, A., Prysak, M., Herron, B. J. and Beier, D. R. (2010). Prdm16 is required for normal palatogenesis in mice. *Hum. Mol. Genet.* **19**, 774-789. doi:10.1093/hmg/ddp543

Bogdanovic, O., Fernandez-Miñán, A., Tena, J. J., De La Calle-Mustienes, E., Hidalgo, C., Van Kruysbergen, I., Van Heeringen, S. J., Veenstra, G. J. C. and Gómez-Skarmeta, J. L. (2012). Dynamics of enhancer chromatin signatures mark the transition from pluripotency to cell specification during embryogenesis. *Genome Res.* **22**, 2043-2053. doi:10.1101/gr.134833.111

Buenrostro, J. D., Wu, B., Chang, H. Y. and Greenleaf, W. J. (2015). ATAC-seq: a method for assaying chromatin accessibility genome-wide. *Curr. Protoc. Mol. Biol.* **109**, 21 29 1-21 29 9. doi:10.1002/0471142727.mb2129s109

Cantu, C., Felker, A., Zimmerli, D., Prummel, K. D., Cabello, E. M., Chiavacci, E., MÃ©Ndez-Acevedo, K. M., Kirchgeorg, L., Burger, S., Ripoll, J. et al. (2018). Mutations in Bcl9 and Pygo genes cause congenital heart defects by tissue-specific perturbation of Wnt/beta-catenin signaling. *Genes Dev.* **32**, 1443-1458. doi:10.1101/gad.315531.118

Carney, T. J., Dutton, K. A., Greenhill, E., Delfino-Machín, M., Dufourcq, P., Blader, P. and Kelsh, R. N. (2006). A direct role for Sox10 in specification of neural crest-derived sensory neurons. *Development* **133**, 4619-4630. doi:10.1242/dev.02668

Chai, Y., Jiang, X., Ito, Y., Bringas, P., Han, J., Rowitch, D. H., Soriano, P., Mcmahon, A. P. and Sucov, H. M. (2000). Fate of the mammalian cranial neural crest during tooth and mandibular morphogenesis. *Development* **127**, 1671-1679. doi:10.1242/dev.127.8.1671

Chen, B., Dodge, M. E., Tang, W., Lu, J., Ma, Z., Fan, C.-W., Wei, S., Hao, W., Kilgore, J., Williams, N. S. et al. (2009). Small molecule-mediated disruption of Wnt-dependent signaling in tissue regeneration and cancer. *Nat. Chem. Biol.* **5**, 100-107. doi:10.1038/nchembio.137

Danielian, P. S., Muccino, D., Rowitch, D. H., Michael, S. K. and Mcmahon, A. P. (1998). Modification of gene activity in mouse embryos in utero by a tamoxifen-inducible form of Cre recombinase. *Curr. Biol.* **8**, 1323-1326. doi:10.1016/S0960-9822(07)00562-3

Davis, L. A. and Zur Nieden, N. I. (2008). Mesodermal fate decisions of a stem cell: the Wnt switch. *Cell. Mol. Life Sci.* **65**, 2658-2674. doi:10.1007/s00018-008-8042-1

Day, T. F., Guo, X., Garrett-Beal, L. and Yang, Y. (2005). Wnt/β-catenin signaling in mesenchymal progenitors controls osteoblast and chondrocyte differentiation during vertebrate skeletogenesis. *Dev. Cell* **8**, 739-750. doi:10.1016/j.devcel.2005.03.016

Ding, H. L., Clouthier, D. E. and Artinger, K. B. (2013). Redundant roles of PRDM family members in zebrafish craniofacial development. *Dev. Dyn.* **242**, 67-79. doi:10.1002/dvdy.23895

Di Zazzo, E., De Rosa, C., Abbondanza, C. and Moncharmont, B. (2013). PRDM Proteins: molecular mechanisms in signal transduction and transcriptional regulation. *Biology (Basel)* **2**, 107-141. doi:10.3390/biology2010107

Dutton, J. R., Antonellis, A., Carney, T. J., Rodrigues, F. S. L. M., Pavan, W. J., Ward, A. and Kelsh, R. N. (2008). An evolutionarily conserved intronic region controls the spatiotemporal expression of the transcription factor Sox10. *BMC Dev. Biol.* **8**, 105. doi:10.1186/1471-213X-8-105

Fog, C. K., Galli, G. G. and Lund, A. H. (2012). PRDM proteins: important players in differentiation and disease. *BioEssays* **34**, 50-60. doi:10.1002/bies.201100107

Goyama, S. and Kurokawa, M. (2010). Evi-1 as a critical regulator of leukemic cells. *Int. J. Hematol.* **91**, 753-757. doi:10.1007/s12185-010-0618-5

Goyama, S., Yamamoto, G., Shimabe, M., Sato, T., Ichikawa, M., Ogawa, S., Chiba, S. and Kurokawa, M. (2008). Evi-1 is a critical regulator for hematopoietic stem cells and transformed leukemic cells. *Cell Stem Cell* **3**, 207-220. doi:10.1016/j.stem.2008.06.002

Hall, B. K. (1978a). *Developmental and Cellular Skeletal Biology*. New York: Academic Press.

Hall, B. K. (1978b). Initiation of osteogenesis by mandibular mesenchyme. *Arch. Oral Biol.* **23**, 1157-1161. doi:10.1016/0003-9969(78)90124-3

Harms, M. J., Lim, H.-W., Ho, Y., Shapira, S. N., Ishibashi, J., Rajakumari, S., Steger, D. J., Lazar, M. A., Won, K.-J. and Seale, P. (2015). PRDM16 binds MED1 and controls chromatin architecture to determine a brown fat transcriptional program. *Genes Dev.* **29**, 298-307. doi:10.1101/gad.252734.114

Harris, M. A., Clark, J., Ireland, A., Lomax, J., Ashburner, M., Foulger, R., Eilbeck, K., Lewis, S., Marshall, B., Mungall, C. et al. (2004). The Gene Ontology (GO) database and informatics resource. *Nucleic Acids Res.* **32**, D258-D261. doi:10.1093/nar/gkh066

Hartmann, C. and Tabin, C. J. (2000). Dual roles of Wnt signaling during chondrogenesis in the chicken limb. *Development* **127**, 3141-3159. doi:10.1242/dev.127.14.3141

Heinz, S., Benner, C., Spann, N., Bertolino, E., Lin, Y. C., Laslo, P., Cheng, J. X., Murre, C., Singh, H. and Glass, C. K. (2010). Simple combinations of lineage-determining transcription factors prime cis-regulatory elements required for macrophage and B cell identities. *Mol. Cell* **38**, 576-589. doi:10.1016/j.molcel.2010.05.004

Hill, T. P., SpÃ¤Ter, D., Taketo, M. M., Birchmeier, W. and Hartmann, C. (2005). Canonical Wnt/beta-catenin signaling prevents osteoblasts from differentiating into chondrocytes. *Dev. Cell* **8**, 727-738. doi:10.1016/j.devcel.2005.02.013

Hohenauer, T. and Moore, A. W. (2012). The Prdm family: expanding roles in stem cells and development. *Development* **139**, 2267-2282. doi:10.1242/dev.070110

Hoyt, P. R., Bartholomew, C., Davis, A. J., Yutzey, K., Gamer, L. W., Potter, S. S., Ihle, J. N. and Mucenski, M. L. (1997). The Evi1 proto-oncogene is required at midgestation for neural, heart, and paraxial mesenchyme development. *Mech. Dev.* **65**, 55-70. doi:10.1016/S0925-4773(97)00057-9

Hwang, S. G., Yu, S.-S., Ryu, J.-H., Jeon, H.-B., Yoo, Y.-J., Eom, S.-H. and Chun, J.-S. (2005). Regulation of beta-catenin signaling and maintenance of chondrocyte differentiation by ubiquitin-independent proteasomal degradation of alpha-catenin. *J. Biol. Chem.* **280**, 12758-12765. doi:10.1074/jbc.M413367200

Jones, F. S., Kioussi, C., Copertino, D. W., Kallunki, P., Holst, B. D. and Edelman, G. M. (1997). Barx2, a new homeobox gene of the Bar class, is expressed in neural and craniofacial structures during development. *Proc. Natl. Acad. Sci. USA* **94**, 2632-2637. doi:10.1073/pnas.94.6.2632

Joyner, A. and Wall, N. (2008). Immunohistochemistry of whole-mount mouse embryos. *CSH Protoc* **2008**, pdb prot4820.

Jugessur, A., Shi, M., Gjessing, H. K., Lie, R. T., Wilcox, A. J., Weinberg, C. R., Christensen, K., Boyles, A. L., Daack-Hirsch, S., Nguyen, T. T. et al. (2010). Maternal genes and facial clefts in offspring: a comprehensive search for genetic associations in two population-based cleft studies from Scandinavia. *PLoS ONE* **5**, e11493. doi:10.1371/journal.pone.0011493

Kajimura, S., Seale, P., Kubota, K., Lunsford, E., Frangioni, J. V., Gygi, S. P. and Spiegelman, B. M. (2009). Initiation of myoblast to brown fat switch by a PRDM16-C/EBP-beta transcriptional complex. *Nature* **460**, 1154-1158. doi:10.1038/nature08262

Kajimura, S., Seale, P., Tomaru, T., Erdjument-Bromage, H., Cooper, M. P., Ruas, J. L., Chin, S., Tempst, P., Lazar, M. A. and Spiegelman, B. M. (2008). Regulation of the brown and white fat gene programs through a PRDM16/CtBP transcriptional complex. *Genes Dev.* **22**, 1397-1409. doi:10.1101/gad.1666108

Keith, A. (1910). Abnormal ossification of Meckel's cartilage. *J. Anat. Physiol.* **44**, 151-152.

Keller, R., Davidson, L., Edlund, A., Elul, T., Ezin, M., Shook, D. and Skoglund, P. (2000). Mechanisms of convergence and extension by cell intercalation. *Philos. Trans. R. Soc. Lond. B Biol. Sci.* **355**, 897-922. doi:10.1098/rstb.2000.0626

Kimmel, C. B., Ballard, W. W., Kimmel, S. R., Ullmann, B. and Schilling, T. F. (1995). Stages of embryonic development of the zebrafish. *Dev. Dyn.* **203**, 253-310. doi:10.1002/aja.1002030302

Kimmel, C. B., Miller, C. T., Kruze, G., Ullmann, B., Bremiller, R. A., Larison, K. D. and Snyder, H. C. (1998). The shaping of pharyngeal cartilages during early development of the zebrafish. *Dev. Biol.* **203**, 245-263. doi:10.1006/dbio.1998.9016

Kimmel, C. B., Delaurier, A., Ullmann, B., Dowd, J. and Mcfadden, M. (2010). Modes of developmental outgrowth and shaping of a craniofacial bone in zebrafish. *PLoS ONE* **5**, e9475. doi:10.1371/journal.pone.0009475

Kurokawa, M., Mitani, K., Irie, K., Matsuyama, T., Takahashi, T., Chiba, S., Yazaki, Y., Matsumoto, K. and Hirai, H. (1998). The oncoprotein Evi-1 represses TGF-beta signalling by inhibiting Smad3. *Nature* **394**, 92-96. doi:10.1038/27945

Langmead, B. and Salzberg, S. L. (2012). Fast gapped-read alignment with Bowtie 2. *Nat. Methods* **9**, 357-359. doi:10.1038/nmeth.1923

Langmead, B., Wilks, C., Antonescu, V. and Hancock, J. (2019). Scaling read aligners to hundreds of threads on general-purpose processors. *Bioinformatics* **35**, 421-432. doi:10.1093/bioinformatics/bty648

Lawson, N. D. and Weinstein, B. M. (2002). In vivo imaging of embryonic vascular development using transgenic zebrafish. *Dev. Biol.* **248**, 307-318. doi:10.1006/dbio.2002.0711

Lei, R., Zhang, K., Liu, K., Shao, X., Ding, Z., Wang, F., Hong, Y., Zhu, M., Li, H. and Li, H. (2016). Transferrin receptor facilitates TGF-beta and BMP signaling activation to control craniofacial morphogenesis. *Cell Death Dis.* **7**, e2282. doi:10.1038/cddis.2016.170

Le Pabic, P., Ng, C. and Schilling, T. F. (2014). Fat-Dachsous signaling coordinates cartilage differentiation and polarity during craniofacial development. *PLoS Genet.* **10**, e1004726. doi:10.1371/journal.pgen.1004726

Li, Y., Zhao, W., Li, D., Tao, X., Xiong, Z., Liu, J., Zhang, W., Ji, A., Tang, K., Liu, F. et al. (2019). EDAR, LYPLAL1, PRDM16, PAX3, DKK1, TNFSF12, CACNA2D3, and SUPT3H gene variants influence facial morphology in a Eurasian population. *Hum. Genet.* **138**, 681-689. doi:10.1007/s00439-019-02023-7

Liu, Y. and Xiao, A. (2011). Epigenetic regulation in neural crest development. *Birth Defects Res. A Clin. Mol. Teratol* **91**, 788-796. doi:10.1002/bdra.20797

Liu, F., Van Der Lijn, F., Schurmann, C., Zhu, G., Chakravarty, M. M., Hysi, P. G., Wollstein, A., Lao, O., De Bruijne, M., Ikram, M. A. et al. (2012). A genome-wide association study identifies five loci influencing facial morphology in Europeans. *PLoS Genet.* **8**, e1002932. doi:10.1371/journal.pgen.1002932

Liu, H., Duncan, K., Helverson, A., Kumari, P., Mumm, C., Xiao, Y., Carlson, J. C., Darbellay, F., Visel, A., Leslie, E. et al. (2020). Analysis of zebrafish periderm enhancers facilitates identification of a regulatory variant near human KRT8/18. *Elife* **9**, e51325. doi:10.7554/eLife.51325.sa2

Manocha, S., Farokhnia, N., Khosropanah, S., Bertol, J. W., Santiago, J. and Fakhouri, W. D. (2019). Systematic review of hormonal and genetic factors involved in the nonsyndromic disorders of the lower jaw. *Dev. Dyn.* **248**, 162-172. doi:10.1002/dvdy.8

Martin, M. (2011). Cutadapt removes adapter sequences from high-throughput sequencing reads. *EMBnet.journal* **17**, 3. doi:10.14806/ej.17.1.200

Meech, R., Edelman, D. B., Jones, F. S. and Makarenkova, H. P. (2005). The homeobox transcription factor Barx2 regulates chondrogenesis during limb development. *Development* **132**, 2135-2146. doi:10.1242/dev.01811

Mi, H., Muruganujan, A., Ebert, D., Huang, X. and Thomas, P. D. (2019a). PANTHER version 14: more genomes, a new PANTHER GO-slim and improvements in enrichment analysis tools. *Nucleic Acids Res.* **47**, D419-D426. doi:10.1093/nar/gky1038

Mi, H., Muruganujan, A., Huang, X., Ebert, D., Mills, C., Guo, X. and Thomas, P. D. (2019b). Protocol Update for large-scale genome and gene function analysis with the PANTHER classification system (v.14.0). *Nat. Protoc.* **14**, 703-721. doi:10.1038/s41596-019-0128-8

Moldes, M., Zuo, Y., Morrison, R. F., Silva, D., Park, B.-H., Liu, J. and Farmer, S. R. (2003). Peroxisome-proliferator-activated receptor gamma suppresses Wnt/beta-catenin signalling during adipogenesis. *Biochem. J.* **376**, 607-613. doi:10.1042/bj20030426

Moro, E., Ozhan-Kizil, G., Mongera, A., Beis, D., Wierzbicki, C., Young, R. M., Bournele, D., Domenichini, A., Valdivia, L. E., Lum, L. et al. (2012). In vivo Wnt signaling tracing through a transgenic biosensor fish reveals novel activity domains. *Dev. Biol.* **366**, 327-340. doi:10.1016/j.ydbio.2012.03.023

Navajas Acedo, J., Voas, M. G., Alexander, R., Woolley, T., Unruh, J. R., Li, H., Moens, C. and Piotrowski, T. (2019). PCP and Wnt pathway components act in parallel during zebrafish mechanosensory hair cell orientation. *Nat. Commun.* **10**, 3993. doi:10.1038/s41467-019-12005-y

Palmer, S., Brouillet, J.-P., Kilbey, A., Fulton, R., Walker, M., Crossley, M. and Bartholomew, C. (2001). Evi-1 transforming and repressor activities are mediated by CtBP co-repressor proteins. *J. Biol. Chem.* **276**, 25834-25840. doi:10.1074/jbc.M102343200

Ramaesh, T. and Bard, J. B. (2003). The growth and morphogenesis of the early mouse mandible: a quantitative analysis. *J. Anat.* **203**, 213-222. doi:10.1046/j.1469-7580.2003.00210.x

Ramirez, F., Ryan, D. P., Grüning, B., Bhardwaj, V., Kilpert, F., Richter, A. S., Heyne, S., Dündar, F. and Manke, T. (2016). deepTools2: a next generation web server for deep-sequencing data analysis. *Nucleic Acids Res.* **44**, W160-W165. doi:10.1093/nar/gkw257

Ricks, J. E., Ryder, V. M., Bridgewater, L. C., Schaalje, B. and Seegmiller, R. E. (2002). Altered mandibular development precedes the time of palate closure in mice homozygous for disproportionate micromelia: an oral clefting model supporting the Pierre-Robin sequence. *Teratology* **65**, 116-120. doi:10.1002/tera.10022

Ross-Innes, C. S., Stark, R., Teschendorff, A. E., Holmes, K. A., Ali, H. R., Dunning, M. J., Brown, G. D., Gojis, O., Ellis, I. O., Green, A. R. et al. (2012). Differential oestrogen receptor binding is associated with clinical outcome in breast cancer. *Nature* **481**, 389-393. doi:10.1038/nature10730

Ryu, J. H., Kim, S. J., Kim, S. H., Oh, C. D., Hwang, S. G., Chun, C. H., Oh, S. H., Seong, J. K., Huh, T. L. and Chun, J. S. (2002). Regulation of the chondrocyte phenotype by beta-catenin. *Development* **129**, 5541-5550. doi:10.1242/dev.00110

Sato, T., Goyama, S., Nitta, E., Takeshita, M., Yoshimi, M., Nakagawa, M., Kawazu, M., Ichikawa, M. and Kurokawa, M. (2008). Evi-1 promotes para-aortic splanchnopleural hematopoiesis through up-regulation of GATA-2 and repression of TGF-b signaling. *Cancer Sci.* **99**, 1407-1413. doi:10.1111/j.1349-7006.2008.00842.x

Seale, P., Bjork, B., Yang, W., Kajimura, S., Chin, S., Kuang, S., Scimè, A., Devarakonda, S., Conroe, H. M., Erdjument-Bromage, H. et al. (2008). PRDM16 controls a brown fat/skeletal muscle switch. *Nature* **454**, 961-967. doi:10.1038/nature07182

Seale, P., Kajimura, S., Yang, W., Chin, S., Rohas, L. M., Uldry, M., Tavernier, G., Langin, D. and Spiegelman, B. M. (2007). Transcriptional control of brown fat determination by PRDM16. *Cell Metab.* **6**, 38-54. doi:10.1016/j.cmet.2007.06.001

Shaffer, J. R., Orlova, E., Lee, M. K., Leslie, E. J., Raffensperger, Z. D., Heike, C. L., Cunningham, M. L., Hecht, J. T., Kau, C. H., Nidey, N. L. et al. (2016). Genome-wide association study reveals multiple loci influencing normal human facial morphology. *PLoS Genet.* **12**, e1006149. doi:10.1371/journal.pgen.1006149

Shull, L. C., Sen, R., Menzel, J., Goyama, S., Kurokawa, M. and Artinger, K. B. (2020). The conserved and divergent roles of Prdm3 and Prdm16 in zebrafish and mouse craniofacial development. *Dev. Biol.* **461**, 132-144. doi:10.1016/j.ydbio.2020.02.006

Skene, P. J. and Henikoff, S. (2017). An efficient targeted nuclease strategy for high-resolution mapping of DNA binding sites. *Elife* **6**, e21856. doi:10.7554/eLife.21856

Sun, X., Zhang, R., Chen, H., Du, X., Chen, S., Huang, J., Liu, M., Xu, M., Luo, F., Jin, M. et al. (2020). Fgfr3 mutation disrupts chondrogenesis and bone ossification in zebrafish model mimicking CATSHL syndrome partially via enhanced Wnt/beta-catenin signaling. *Theranostics* **10**, 7111-7130. doi:10.7150/thno.45286

Svandova, E., Anthwal, N., Tucker, A. S. and Matalova, E. (2020). Diverse fate of an enigmatic structure: 200 years of Meckel's cartilage. *Front. Cell Dev. Biol.* **8**, 821. doi:10.3389/fcell.2020.00821

Takada, I., Kouzmenko, A. P. and Kato, S. (2010). PPAR-gamma signaling crosstalk in mesenchymal stem cells. *PPAR Research* **2010**, 341671. doi:10.1155/2010/341671

Trapnell, C., Pachter, L. and Salzberg, S. L. (2009). TopHat: discovering splice junctions with RNA-Seq. *Bioinformatics* **25**, 1105-1111. doi:10.1093/bioinformatics/btp120

Trapnell, C., Roberts, A., Goff, L., Pertea, G., Kim, D., Kelley, D. R., Pimentel, H., Salzberg, S. L., Rinn, J. L. and Pachter, L. (2012). Differential gene and transcript expression analysis of RNA-seq experiments with TopHat and Cufflinks. *Nat. Protoc.* **7**, 562-578. doi:10.1038/nprot.2012.016

Vervoort, M., Meulemeester, D., Béhague, J. and Kerner, P. (2016). Evolution of Prdm genes in animals: insights from comparative genomics. *Mol. Biol. Evol.* **33**, 679-696. doi:10.1093/molbev/msv260

Walker, M. B. and Kimmel, C. B. (2007). A two-color acid-free cartilage and bone stain for zebrafish larvae. *Biotech. Histochem.* **82**, 23-28. doi:10.1080/10520290701333558

Wallin, J., Wilting, J., Koseki, H., Fritsch, R., Christ, B. and Balling, R. (1994). The role of Pax-1 in axial skeleton development. *Development* **120**, 1109-1121. doi:10.1242/dev.120.5.1109

Warner, D. R., Horn, K. H., Mudd, L., Webb, C. L., Greene, R. M. and Pisano, M. M. (2007). PRDM16/MEL1: a novel Smad binding protein expressed in murine embryonic orofacial tissue. *Biochim. Biophys. Acta* **1773**, 814-820. doi:10.1016/j.bbamcr.2007.03.016

Warner, D. R., Wells, J. P., Greene, R. M. and Pisano, M. M. (2013). Gene expression changes in the secondary palate and mandible of Prdm16(−/−) mice. *Cell Tissue Res.* **351**, 445-452. doi:10.1007/s00441-012-1525-2

Westerfield, M. (2007). *The Zebrafish Book: A Guide for the Laboratory Use of Zebrafish (Danio rerio)*. University of Oregon Press.

White, J. D., Indencleef, K., Naqvi, S., Eller, R. J., Hoskens, H., Roosenboom, J., Lee, M. K., Li, J., Mohammed, J., Richmond, S. et al. (2021). Insights into the genetic architecture of the human face. *Nat. Genet.* **53**, 45-53. doi:10.1038/s41588-020-00741-7

Willert, K. and Nusse, R. (1998). Beta-catenin: a key mediator of Wnt signaling. *Curr. Opin. Genet. Dev.* **8**, 95-102. doi:10.1016/S0959-437X(98)80068-3

Wilson, J. and Tucker, A. S. (2004). Fgf and Bmp signals repress the expression of Bapx1 in the mandibular mesenchyme and control the position of the developing jaw joint. *Dev. Biol.* **266**, 138-150. doi:10.1016/j.ydbio.2003.10.012